Citation:
P. Maragos, "Partial Differential Equations for Morphological Scale-Spaces and Eikonal Applications",
in *Image and Video Processing Handbook (Second Edition)*, edited by A. C. Bovik,
Academic Press, 2005, pp.587-612.
DOI: https://doi.org/10.1016/B978-012119792-6/50098-X

PDEs for Morphological Scale-Spaces and Eikonal Applications

Petros Maragos

National Technical University of Athens
School of Electrical & Computer Engineering
Zografou 15773, Athens, Greece.
Email: maragos@cs.ntua.gr

1 Introduction

In contrast to the all-discrete approaches that dominated image processing in the recent past, in computer vision since the mid 1980's there have been proposed continuous models for several vision tasks based on *partial differential equations (PDEs)*. The discrete part of such approaches comes only in the corresponding difference equations (numerical algorithms) that approximate the solution of these PDEs. Motivations for using PDEs in image analysis and vision include better and more intuitive mathematical modeling, connections with physics, better approximation to the Euclidean geometry of the problem, and existence of efficient numerical algorithms for solving them. One major effort [31] was the use of PDEs in problems of shape from shading and optical flow. However, the most well known vision problem modeled via PDEs is that of multiscale image analysis, i.e. *scale-spaces*. While many such continuous approaches have been linear, the majority and the most useful ones are nonlinear.

Several classes of nonlinear PDEs used in image analysis and vision are based on or related to morphological operations. Morphological image processing has been based traditionally on modeling images as sets or as points in a complete lattice of functions and viewing morphological image transformations as set or lattice operators. Thus, the two classic approaches to analyze or design the deterministic systems of mathematical morphology have been (i) *geometry* by viewing them as image set transformations in Euclidean spaces and (ii) *algebra* to analyze their properties using set or lattice theory. Geometry was used mainly for intuitive understanding, and algebra was restricted to the space domain. Despite their limitations, these approaches have produced a powerful and self-contained broad collection of nonlinear image analysis concepts, operators and algorithms, which have found a broad range of applications in image processing and computer vision; see [73, 49, 28] and Chapter 3.3 of this book for surveys and references. In parallel to these directions, there is a growing part of morphological image processing that is based on ideas from differential calculus and dynamical systems. It combines some early ideas on morpholological signal gradients and some recent ideas on using differential equations to model nonlinear multiscale processes or distance propagation in images. In this chapter we present a unified view of the various interrelated ideas in this area, using occasionally some systems analysis tools in both the space and the slope transform domain.

Among the few early connections between morphology and calculus were the *morphological gradients*. Specifically, given a function $f : \mathbb{R}^m \to \mathbb{R}$, with $m = 1, 2$, its isotropic *morphological sup-derivative* at a point x is defined by

$$\mathcal{M}f(x) \triangleq \lim_{r \downarrow 0} \frac{\sup_{||y|| \le r}\{f(x+y) :\} - f(x)}{r} \tag{1}$$

The derivative $\mathcal{M}$ has been used in morphological image analysis for edge detection. It actually becomes equal to $||\nabla f||$ when f is differentiable.

A broader area where calculus-based ideas have been used in morphology is that of *multiscale image analysis*. Detecting features, structure, objects and generally modeling many visual information extraction tasks has necessitated the analysis of image signals at multiple scales. Following the initial formulation of multiscale image analysis using Gaussian convolutions by Marr and his co-workers [50], two other important developments were the continuous Gaussian scale-space by Witkin [84] and the observation by Koenderink [37] that this scale-space can be modeled via the heat diffusion PDE. Specifically, if $u(x,y,t) = f(x,y) * G_t(x,y)$ is the multiscale linear convolution of an original image signal $f(x,y)$ with a Gaussian function $G_t(x,y) = \exp[-(x^2+y^2)/4t]/4\pi t$ whose variance is proportional to scale t, then the scale-space function u can be generated from the isotropic and homogeneous heat diffusion PDE[1]

$$u_t = \nabla^2 u \tag{2}$$

with initial condition $u(x,y,0) = f(x,y)$. The popularity of this approach is due to its linearity and relations to the heat PDE about which much is known from physics and mathematics. The big disadvantage of the Gaussian scale-space approach is the fact that linear smoothers blur and shift important image features, e.g., edges, as shown in Fig. 1. There are, however, several classes of *nonlinear smoothing* filters that can smooth while preserving important image features and can provide a nonlinear scale-space. A large such class consists of morphological *openings* and *closings*. These can be of a simple type, i.e. serial compositions of Minkowski erosions and dilations in a multiscale formulation [51, 73, 43] or an advanced type like the *reconstruction* filters [69, 56]. Figure 1 shows examples of two such types of *clos-openings* (i.e., compositions of openings and closings): 1) Flat Minkowski clos-openings by a 2D disk-like structuring element which preserve the vertical image edges but may distort horizontal edges (contours) by fitting the shape of the structuring element. 2) Graylevel reconstruction clos-openings which, starting from a reference image and a marker, can reconstruct whole objects hit by the marker with exact preservation of their boundaries while suppressing all other surrounding objects inside which the marker cannot fit; the marker for the reconstruction opening (closing) was an erosion (dilation) of the original image by a disk of radius equal to scale.

As was done for linear scale-spaces [50, 84], there has been much work on tracking the evolution of important image features through morphological scale-spaces. Examples include size distributions with multiscale openings [73, 43], zero-crossings of multiscale 1D openings [63], extrema of multiscale dilations-erosions [33], and peaks of multiscale 1D open-closings [5].

Until recently the vast majority of implementations of multiscale morphological filtering had been discrete. In 1992 three teams of researchers independently published nonlinear PDEs that model the continuous morphological scale-space. Brockett and Maragos [11] developed nonlinear PDEs that model multiscale morphological dilation, erosion, opening and closing by compact-support structuring elements that are either convex sets or concave functions and may have non-smooth boundaries. Their work was based on the semigroup structure of the multiscale dilation and erosion operators and the use of morphological derivatives to deal with the development of shocks. This is the viewpoint from which we present the morphological PDEs in this chapter. Alvarez et al. [1] developed PDE-based models for scale-spaces that satisfy certain axiomatic principles. As part of their general work they obtained PDEs for multiscale flat dilation and erosion by compact convex sets. Boomgaard and Smeulders [79] obtained PDEs for multiscale dilation and erosion by studying the propagation of the boundaries of 2D sets and signal graphs under multiscale dilation and erosion. Their work applies to convex structuring elements whose boundaries contain no linear segments, are smooth and possess a unique normal at each point. Refinements of the above three

[1]Short Notation for PDEs: $u_t = \partial u/\partial t$, $u_x = \partial u/\partial x$, $u_y = \partial u/\partial y$, $\nabla u = (u_x, u_y)$, $\nabla^2 u = u_{xx} + u_{yy}$, $\mathrm{div}((v,w)) = v_x + w_y$.

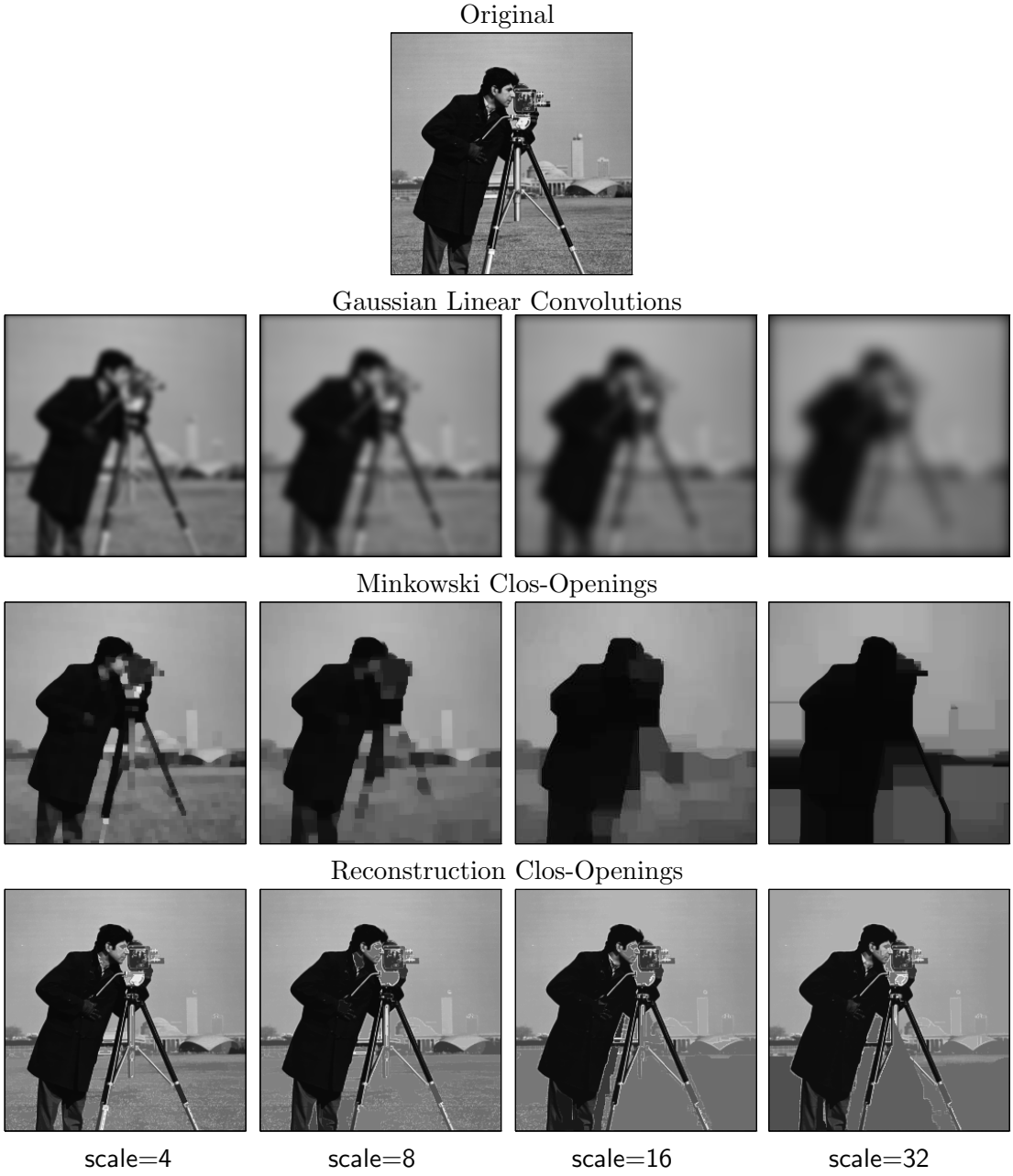

Figure 1: Linear and morphological multiscale image smoothers. (The scale parameter was defined as: the variance of the Gaussians for linear convolutions; the radius of the structuring element for clos-openings; the scale of the marker for the reconstruction filters.)

works for PDEs modelling multiscale morphology followed in [2, 3, 12, 45, 47, 80]. Extensions also followed in several directions including asymptotic analysis and iterated filtering by Guichard & Morel [26, 27], a unification of morphological PDEs using Legendre-Fenchel 'slope' transforms by Heijmans & Maragos [29], a common algebraic framework for linear and morphological scale-spaces by Heijmans & Boomgaard [30], and PDEs for morphological reconstruction operators with global constraints by Maragos and Meyer [56, 46].

To illustrate the basic idea behind morphological PDEs we consider a 1D example shown in Fig. 2, the multiscale flat dilation δ and erosion ε of a 1D signal $f(x)$ at scales $t \geq 0$:

$$\delta(x,t) = \sup_{|y| \leq t} f(x+y), \quad \varepsilon(x,t) = \inf_{|y| \leq t} f(x+y).$$

The PDEs generating these multiscale flat dilations and erosions are

$$\begin{aligned} &\delta_t = |\delta_x|, \quad \varepsilon_t = -|\varepsilon_x|, \\ &\delta(x,0) = \varepsilon(x,0) = f(x). \end{aligned} \tag{3}$$

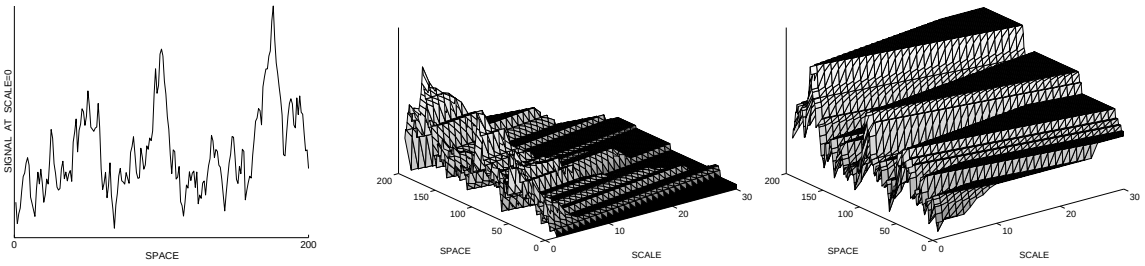

(a) (b) (c)

Figure 2: (a) Original 1D signal $f(x)$ at scale $t = 0$. (b) Multiscale erosion $\varepsilon(x,t) = (f \ominus tB)(x)$, and (c) Multiscale dilation $\delta(x,t) = (f \oplus tB)(x)$ of $f(x)$ by a set $B = [-1,1]$ for scales $t = [0,30]$.

In parallel to the development of the above ideas, there have been some advances in the field of differential geometry for *curve-surface evolution* using *level-set* methods. Specifically, Osher and Sethian [61, 62, 74] have developed PDEs of the Hamilton-Jacobi type to model the propagation of curves embedded as level curves (isoheight contours) of functions evolving in scale-space. Further, they developed robust numerical algorithms to solve these PDEs based on stable and shock-capturing schemes to solve similar shock-producing nonlinear wave PDEs [38]. A broad range of applications to image processing and computer vision has followed since then. Examples include: 1) implementation of continuous-scale morphological dilations and erosions by Arehart et al. [4] and Sapiro et al. [70]; 2) shape analysis by Kimia et al. [34, 77]; 3) geometry-based active contours and related segmentation by Caselles et al [15], Malladi et al. [41], and Yezzi et al. [85]. 4) Weighted distance transforms and related morphological segmentation discussed later in this chapter.

Multiscale dilations and erosions of binary images can also be obtained via distance transforms, i.e., the distance function from the original image set. Discrete distance transforms can be implemented fast via 2D min-sum difference equations developed in [67, 10], which are special cases of recursive erosions. Using Huygen's construction, the boundaries of multiscale dilations/erosions by disks can also be viewed as the wavefronts of a wave initiating from the original image boundary and propagating with constant normal speed in a homogeneous medium [9]. This idea can also be extended to heterogeneous media by using a weighted distance function, where the weights are inversely proportional to the propagation speeds [39]. In geometrical optics, the distance wavefronts are obtained from the isolevel contours of the solution of the eikonal PDE. This ubiquitous PDE has been applied to solving various problems in image analysis and computer vision [31] such as shape-from-shading [68, 36], gridless halftoning, and image segmentation [81, 54, 59, 45, 47].

In this chapter we discuss some close relationships among the PDEs for multiscale morphology, the morphological derivatives, the eikonal PDE of optics, the distance transforms and the difference equations used for numerical implementations. The unifying theme is a collection of nonlinear differential or difference equations modeling the scale-space dynamics of continuous or discrete morphological systems. We call this area *differential morphology*. We also present analysis tools for the nonlinear systems used in differential morphology which have many similarities with the tools used to analyze linear differential schemes. These tools apply either to the space domain or to the slope transform domain.

The chapter is organized as follows. We begin in Section 2 with brief descriptions of analytic methods for 2D morphological systems both in the spatial and the slope domain. In Section 3

we discuss the basic PDEs for multiscale dilations and erosions, refine them using morphological derivatives, give their slope domain interpretation, describe PDEs for object-oriented reconstruction filters, and outline numerical algorithms for their implementation. Section 4 summarizes the main ideas from curve evolution as they apply to differential morphology. Section 5 deals with distance transforms for binary images and the analysis of their computation methods based on min-sum difference equations and slope filters. The eikonal PDE and its solution via weighted distance transforms are discussed in Section 6. Finally, Section 7.4 presents an introduction to image segmentation by using the eikonal PDE and curve evolution.

Additional material on nonlinear PDEs and curve evolution as applied to image processing can be found in this book in Chapter 4.14 by Acton, in Chapter 4.15 by Guichard et al. and in Chapter 4.17 by Caselles et al.

2 Multidimensional Morphological Systems and Slope Transforms

The space domain on which images are defined can be either continuous $\mathbb{E} = \mathbb{R}^m$ or discrete $\mathbb{E} = \mathbb{Z}^m$, $m = 1, 2, 3$. The signal range is generally a subset of $\overline{\mathbb{R}} = \mathbb{R} \cup \{-\infty, +\infty\}$. On the lattice of all signals $f : \mathbb{E} \to \overline{\mathbb{R}}$ equipped with pointwise supremum $\bigvee$, infimum $\bigwedge$ and partial ordering $\leq$, a signal operator or system $\Psi : f \mapsto \Psi(f)$ is generally called: *Dilation* if $\Psi(\bigvee_i f_i) = \bigvee_i \Psi(f_i)$ and *Erosion* if $\Psi(\bigwedge_i f_i) = \bigwedge_i \Psi(f_i)$ for any signal collection $\{f_i\}$; *Opening* if Ψ is increasing w.r.t. $\leq$, idempotent $[\Psi(\Psi(f)) = \Psi(f)]$ and anti-extensive $[f \leq \Psi(f)]$; *Closing* if Ψ is increasing, idempotent and extensive; *Translation-invariant* if $\Psi[c + f(x - y)] = c + \Psi(f)(x - y)$, for any f, y, c.

The classic morphological signal convolutions are the *Minkowski weighted dilation* $\oplus$ and *weighted erosion* $\ominus$ of an image f by a structuring function (kernel) g:

$$\begin{array}{rcl} (f \oplus g)(x) & \triangleq & \bigvee_{y \in \mathbb{E}} f(y) + g(x - y) \\ (f \ominus g)(x) & \triangleq & \bigwedge_{y \in \mathbb{E}} f(y) - g(y - x) \end{array} \tag{4}$$

The scalar addition in $\overline{\mathbb{R}}$ is like addition in $\mathbb{R}$ extended by the rules $r \pm \infty = \pm\infty \ \forall r \in \mathbb{R}$ and $(+\infty) + (-\infty) = -\infty$. In convex analysis [66] and optimization, the operation $\oplus$ is called *supremal convolution*, and an operation closely related to $\ominus$ is the *infimal convolution*

$$(f \oplus' g)(x) \triangleq \bigwedge_{y \in \mathbb{E}} f(y) +' g(x - y) \tag{5}$$

where $+'$ is like the extended addition in $\overline{\mathbb{R}}$ except that $(+\infty) +' (-\infty) = +\infty$. A simple case of the signal dilation and erosion results when g is *flat*, i.e., equal to 0 over its support set B and $-\infty$ elsewhere. Then the weighted dilation and erosion of f by g reduce to the *flat* dilation and erosion of f by B:

$$\begin{array}{rcl} (f \oplus B)(x) & \triangleq & \bigvee_{y \in B} f(x - y) \\ (f \ominus B)(x) & \triangleq & \bigwedge_{y \in B} f(x + y) \end{array} \tag{6}$$

An alternative construction of the flat operations is to extend set operators to image function operators by using level sets and threshold superposition [73, 42, 28]. Specifically, if for $\lambda \in \mathbb{R}$

$$X_\lambda(f) \triangleq \{x \in \mathbb{E} : f(x) \geq \lambda\} \tag{7}$$

are the *upper level sets* of an image function f, and we are given an increasing set operator Ψ, then we can construct a so-called **flat operator**

$$\psi(f) = \sup\{\lambda \in \mathbb{R} : x \in \Psi(X_\lambda(f))\} \tag{8}$$

via *threshold superposition* of the outputs of the set operator acting on all input level sets. The flat operator ψ can process both binary and graylevel images. For example, if Ψ is the Minkowski set dilation or erosion by a disk B, then the corresponding flat operator ψ becomes the flat dilation and erosion of f by B in (6).

2.1 Morphological Systems

Of particular interest in this chapter are operators $\mathcal{E} : f \mapsto \mathcal{E}(f)$ that are **erosion and translation-invariant (ETI)** systems. Such systems obey an infimum-of-sums superposition:

$$\mathcal{E}[\bigwedge_i c_i + f_i(x)] = \bigwedge_i c_i + \mathcal{E}[f_i(x)] \tag{9}$$

Similarly, **dilation and translation-invariant (DTI)** systems obey a supremum-of-sums superposition as in Eq. (9) but with $\bigwedge$ replaced by $\bigvee$. An elementary signal useful for analyzing such systems is the *zero impulse*

$$\xi_\wedge(x) \triangleq \begin{cases} 0, & x = 0 \\ \infty, & x \neq 0 \end{cases}$$

Occasionally we shall refer to $\xi_\wedge$ as a 'lower' impulse and to its negated version $\xi_\vee(x) = -\xi_\wedge(x)$ as an 'upper' impulse. If we define the lower **impulse response** of an ETI system $\mathcal{E}$ as its output $g = \mathcal{E}(\xi_\wedge)$ when the input is the lower impulse, we find that the system's action is equivalent to the infimal convolution of the input with its lower impulse response [44]:

$$\mathcal{E} \text{ is ETI} \Longleftrightarrow \mathcal{E}(f) = f \oplus' g, \quad g = \mathcal{E}(\xi_\wedge).$$

Similarly, a system $\mathcal{D}$ is DTI iff $\mathcal{D}(f) = f \oplus h$, where $h = \mathcal{D}(\xi_\vee)$ is the system's upper impulse response. Thus, DTI and ETI systems are uniquely determined in the spatial domain by their impulse responses, which also control their causality and stability.

Next we shall create a *transform domain* for morphological systems. Let $< \alpha, x > \triangleq \sum_{i=1}^m \alpha_i x_i$ denote the inner product of the vectors $\alpha = (\alpha_1, ..., \alpha_m)$ and $x = (x_1, ..., x_m)$ in $\mathbb{R}^m$. First note that the hyperplanes $f(x) =< \alpha, x > +c$ are *eigenfunctions* of any DTI system $\mathcal{D}$ or ETI system $\mathcal{E}$ because

$$\begin{aligned} \mathcal{D}[< \alpha, x > +c] &=< \alpha, x > +c + H_\vee(\alpha) \\ \mathcal{E}[< \alpha, x > +c] &=< \alpha, x > +c + G_\wedge(\alpha) \end{aligned} \tag{10}$$

The corresponding *eigenvalues*

$$\begin{aligned} H_\vee(\alpha) &\triangleq \bigvee_x h(x) - < \alpha, x > \\ G_\wedge(\alpha) &\triangleq \bigwedge_x g(x) - < \alpha, x > \end{aligned} \tag{11}$$

are called, respectively, the upper and lower **slope response** of the DTI and ETI system. They measure the amount of shift in the intercept of the input hyperplanes with slope vector α. They are also conceptually similar to the frequency response of linear systems.

2.2 Slope Transforms

Viewing the slope response as a signal transform with variable the slope vector, we define for any m-dimensional signal $f(x)$ its **upper slope transform** as the m-dimensional function $F_\vee : \mathbb{R}^m \to \overline{\mathbb{R}}$ defined by

$$F_\vee(\alpha) \triangleq \bigvee_{x \in \mathbb{R}^m} f(x) - < \alpha, x > \tag{12}$$

and as its **lower slope transform**[2] the function

$$F_\wedge(\alpha) \triangleq \bigwedge_{x \in \mathbb{R}^m} f(x) - < \alpha, x > \tag{13}$$

[2]In convex analysis [66], given a convex function f there uniquely corresponds another convex function $f^*(\alpha) = \bigvee_x < \alpha, x > -f(x)$ called the *Fenchel conjugate* of f. The lower slope transform of f and its conjugate function are closely related since $f^*(\alpha) = -F_\wedge(\alpha)$.

For a 1D signal $f(x)$, $f(x) - \alpha x$ is the intercept of a line with slope α passing from the point $(x, f(x))$ on the signal's graph. Hence, for each α, the lower slope transform of f is the minimum value of this intercept. For *differentiable*[3] 1D signals, this minimum occurs when the above line becomes a tangent; for 2D signals the tangent line becomes a tangent plane. Examples of 1D lower slope transforms are shown in Fig. 3.

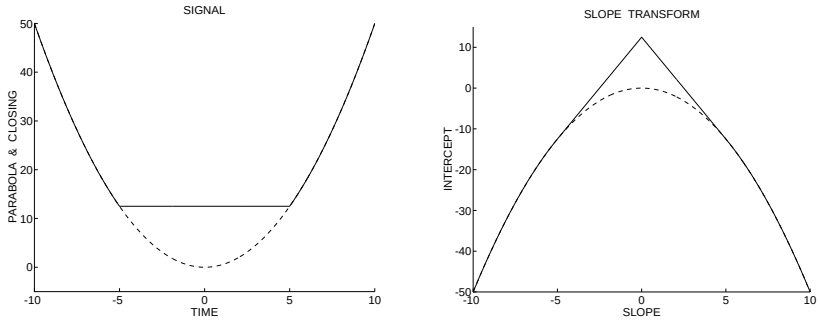

(a) (b)

Figure 3: (a) Convex parabola signal $f(x) = x^2/2$ (in dashed line) and its morphological closing (in solid line) by a flat structuring element $[-5, 5]$. (b) Lower slope transform $F_\wedge(\alpha) = -\alpha^2/2$ of the parabola (in dashed line) and of its closing (in solid line).

In general, a m-dimensional signal $f(x)$ is covered from above by all the hyperplanes $F_\vee(\alpha) + < \alpha, x >$ whose infimum creates an *upper envelope*

$$\text{env}_\vee(f)(x) \triangleq \bigwedge_{\alpha \in \mathbb{R}^m} F_\vee(\alpha) + < \alpha, x > \tag{14}$$

and $f(x)$ is covered from below by hyperplanes $F_\wedge(\alpha) + < \alpha, x >$ whose supremum creates the *lower envelope*

$$\text{env}_\wedge(f)(x) \triangleq \bigvee_{\alpha \in \mathbb{R}^2} F_\wedge(\alpha) + < \alpha, x > \tag{15}$$

We view the signal envelopes $\text{env}_\vee(f)$ and $\text{env}_\wedge(f)$ as the *'inverse'* upper and lower slope transform of f, respectively. One-dimensional examples are shown in Fig. 4. The upper (lower) slope transform is always a convex (concave) function. Similarly, the upper (lower) envelope created by the 'inverse' upper (lower) slope transform is always, a concave (convex) function. Further, for any signal f, $\text{env}_\wedge(f) \leq f \leq \text{env}_\vee(f)$.

The slope transforms have many interesting properties [44, 45, 29]. The most striking is that supremal convolution in the time/space domain corresponds to addition in the slope domain:

$$f(x) \oplus g(x) \quad \overset{\text{Slope Transf.}}{\longleftrightarrow} \quad F_\vee(\alpha) + G_\vee(\alpha)$$

Note the analogy with linear systems where linearly convolving two signals in space corresponds to multiplying their Fourier transforms. Table 1 lists several examples of the 2D upper slope transform. Very similar properties also hold for the 2D lower slope transform, the only differences being the interchange of suprema with infima, concave with convex, and the supremal $\oplus$ with the infimal convolution $\oplus'$.

[3]For differentiable signals, the maximization or minimization of the intercept $f(x) - < \alpha, x >$ involved in both slope transforms can also be done, for a fixed α, by finding its value at the stationary point x^* such that $\nabla f(x^*) = \alpha$. This extreme value of the intercept (as a function of the slope α) is the *Legendre transform* of the signal f. If f is convex (or concave) and has an invertible gradient, its Legendre transform is single-valued and equal to the lower (or upper) transform; otherwise, the Legendre transform is multivalued. This possibly multivalued transform was defined in [21] as a 'slope transform'. Its properties are similar to the properties of the upper/lower slope transform, but there are also some important differences as explained in [44].

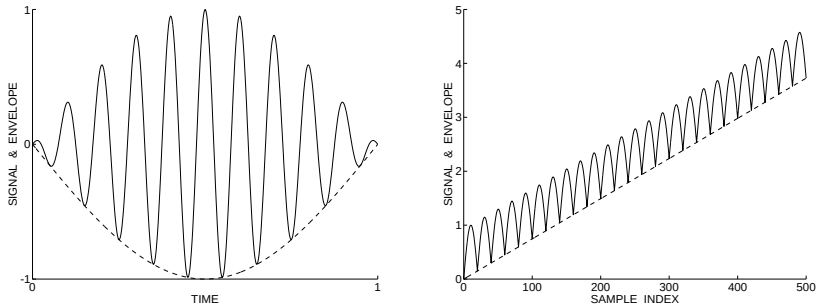

(a) (b)

Figure 4: Signals f (in solid lines) and their lower envelopes $\mathrm{env}_\wedge(f)$ (in dashed lines) obtained via the composition of the lower slope transform and its inverse. (a) Cosine whose amplitude has been modulated by a slower cosine pulse. (b) Impulse response f of a discrete ETI system generated by the min-sum difference equation $f[n] = \min(\xi_\wedge[n], \bigwedge_{1\le k\le 20} f[n-k] + a_k)$, where $a_k = \sin(\pi k/21)$.

Table 1: Examples of 2D Upper Slope Transforms

Signal: $f(x),\ \ x=(x_1,x_2)$	Transform: $F_\vee(\alpha),\ \ \alpha=(\alpha_1,\alpha_2)$
$<\alpha_0, x>$	$-\xi_\vee(\alpha-\alpha_0)$
$<\alpha_0, x> + \zeta_\vee(x)$	$-\zeta_\vee(\alpha-\alpha_0)$
$\xi_\vee(x-x_0)$	$-<\alpha, x_0>$
$\zeta_\vee(x-x_0)$	$-<\alpha, x_0> - \zeta_\vee(\alpha)$
$\begin{cases} 0, & \|\|x\|\|_p \le r \\ -\infty, & \|\|x\|\|_p > r \end{cases}, p\ge 1$	$r\|\|\alpha\|\|_q, \quad \frac{1}{p}+\frac{1}{q}=1$
$-\alpha_0\|\|x\|\|_p, \quad \alpha_0>0$	$\begin{cases} 0, & \|\|\alpha\|\|_q \le \alpha_0 \\ +\infty, & \|\|\alpha\|\|_q > \alpha_0 \end{cases}$
$\sqrt{1-x_1^2-x_2^2}, \quad x_1^2+x_2^2\le 1$	$\sqrt{1+\alpha_1^2+\alpha_2^2}$
$-(x_1^2+x_2^2)/2$	$(\alpha_1^2+\alpha_2^2)/2$
$-(\|x_1\|^p+\|x_2\|^p)/p\ ,\ p>1$	$(\|\alpha_1\|^q+\|\alpha_2\|^q)/q$

$\xi_\vee(x) \triangleq 0$ if $x=0$ and $-\infty$ if $x\ne 0$.
$\zeta_\vee(x) \triangleq 0$ if $x\ge 0$ and $-\infty$ if $x\not\ge 0$.

Given a *discrete-domain* 2D signal $f[i,j]$, we define its lower slope transform by

$$F_\wedge(\alpha_1,\alpha_2) = \bigwedge_{i=-\infty}^{\infty} \bigwedge_{j=-\infty}^{\infty} f[i,j] - (i\alpha_1 + j\alpha_2) \tag{16}$$

and likewise for its upper slope transform using $\bigvee$. The properties of these slope transforms for signals defined on the discrete plane are almost identical to the ones for signals defined on $\mathbb{R}^2$.

Detailed properties and examples of 1D and 2D upper/lower slope transforms can be found in [44, 45]. A more general treatment of slope transforms on complete lattices can be found in [29].

2.3 Min-Sum Difference Equations and Discrete Slope Filters

The space dynamics of a large class of 2D discrete ETI systems can be described by the following general 2D *min-sum difference equation*

$$\begin{aligned} u[i,j] \ &= \ \Big(\textstyle\bigwedge_{(k,\ell)\in M_o} a_{k\ell} +' u[i-k, j-\ell]\Big) \\ &\quad \wedge \Big(\textstyle\bigwedge_{(k,\ell)\in M_i} b_{k\ell} +' f[i-k, j-\ell]\Big) \end{aligned} \tag{17}$$

which we view as a 2D discrete nonlinear system, mapping the input signal f to the output u. The *masks* M_o, M_i are pixel coordinate sets that determine which output and input samples will be added with constant weights to form the current output sample. As explained in [22] for 2D linear difference equations, the recursive computability of Eq. (17) depends on (i) the shape of the output mask $M_o = \{(k,\ell) : a_{k\ell} < +\infty\}$ determining which past output samples are involved in the recursion, (ii) the boundary conditions, i.e., the locations and values of the output samples $y[i,j]$ which are prespecified as initial conditions, and (iii) the scanning order in which the output samples should be computed. We assume boundary conditions of value $+\infty$ and of a shape (dependent on M_o and the scanning order) appropriate so that the difference equation is an ETI system recursively computable. Obviously, $(0,0) \notin M_o$. The nonrecursive part of (17) represents an infimal convolution of the input array $f[i,j]$ with the 2D finite-support structuring function $b[i,j] = b_{ij}$, which is well understood. Thus, we henceforth focus only on the recursive version of Eq. (17) by setting $b_{k\ell} = +\infty$ except from $b_{00} = 0$. This yields the autoregressive 2D min-sum difference equation

$$u[i,j] = (\bigwedge_{(k,\ell)\in M_o} a_{k\ell} +' u[i-k, j-\ell]) \wedge f[i,j] \tag{18}$$

If $g = \mathcal{E}(\xi_\wedge)$ is the impulse response of the corresponding ETI system $\mathcal{E} : f \mapsto u$, then $u = f \oplus' g$. Finding a closed-formula expression for g is generally not possible. However, we can first find the slope response $G_\wedge$ and then, via inverse lower slope transform, find the impulse response g or its envelope $\mathrm{env}_\wedge(g)$.

As shown in [45], the lower slope response is the $0/-\infty$ indicator function $\mathrm{I}_\vee(\cdot)$ of a convex planar region R:

$$\begin{aligned} G_\wedge(\alpha) = \mathrm{I}_\vee(R)(\alpha) &\triangleq \begin{cases} 0, & \alpha \in R \\ -\infty, & \alpha \notin R \end{cases} \\ R &= \{\alpha : <\alpha, (i,j)> \le a_{ij} \ \forall (i,j) \in M_o\} \end{aligned} \tag{19}$$

Thus the system acts as an *ideal-cutoff spatial slope filter* passing all input lower slope vectors α in the planar region R unchanged and rejecting the rest. The inverse slope transform on $G_\wedge$ yields the lower envelope $\mathrm{env}_\wedge(g)$ of the impulse response g. Over short-scale periods g has the shape induced by the sequence $\{a_{ij}\}$. But over scales much longer than the size of the output coefficient mask M_o, g behaves like its lower envelope $\mathrm{env}_\wedge(g)$. See the 1D example of Fig. 4(b). Together $G_\wedge$ and $\mathrm{env}_\wedge(g)$ can describe the long-scale dynamics of the system. In addition, if $g = \mathrm{env}_\wedge(g)$, then the above analysis is also exact for the short-scale behavior.

3 PDEs for Morphological Scale-Spaces

3.1 PDEs for Multiscale Dilations and Erosions

Let $k : \mathbb{R}^2 \to \overline{\mathbb{R}}$ be a unit-scale upper-semicontinuous concave structuring function. Scaling both its values and its support by a scale parameter $t \ge 0$ yields a parameterized family of multiscale structuring functions

$$k_t(x,y) \triangleq \begin{cases} tk(x/t, y/t), & t > 0 \\ \xi_\vee(0,0), & t = 0 \end{cases} \tag{20}$$

which satisfies the semigroup property:

$$k_s \oplus k_t = k_{s+t} \tag{21}$$

Using k_t as the kernel in the basic morphological operations leads to defining the *multiscale dilation* and *erosion* of $f : \mathbb{R}^2 \to \mathbb{R}$ by k_t as the scale-space functions

$$\begin{aligned} \delta(x,y,t) &\triangleq (f \oplus k_t)(x,y) \\ \varepsilon(x,y,t) &\triangleq (f \ominus k_t)(x,y) \end{aligned}$$

where $\delta(x,y,0) = \varepsilon(x,y,0) = f(x,y)$.

In practice, a useful class of functions k consists of *flat* structuring functions

$$k(x,y) = \begin{cases} 0, & (x,y) \in B \\ -\infty, & (x,y) \notin B \end{cases} \tag{22}$$

that are the $0/-\infty$ indicator functions of planar sets B; i.e., $k = \mathrm{I}_\vee(B)$. The general PDE generating the multiscale flat dilations of f by a compact convex symmetric B is [2, 12, 29]

$$\frac{\partial \delta}{\partial t} = \sigma_B\left(\frac{\partial \delta}{\partial x}, \frac{\partial \delta}{\partial y}\right) \tag{23}$$

where σ_B is the *support function* function of B:

$$\sigma_B(x,y) \triangleq \bigvee_{(a,b)\in B} ax + by \tag{24}$$

Useful cases of structuring sets B are obtained by the unit balls $B_p = \{(x,y) : ||(x,y)||_p \leq 1\}$ of the metrics induced by the ℓ_p norms $||\cdot||_p$, for $p = 1, 2, ..., \infty$. The PDEs generating the multiscale flat dilations and erosions of f by B_p are

$$\frac{\partial \delta}{\partial t} = ||\nabla \delta||_q, \quad \frac{\partial \varepsilon}{\partial t} = -||\nabla \varepsilon||_q, \quad \frac{1}{p} + \frac{1}{q} = 1 \tag{25}$$

Examples: Three special cases for $p = 1, 2, \infty$:

$$B = \text{rhombus} \implies \delta_t = \max(|\delta_x|, |\delta_y|) \tag{26}$$

$$B = \text{disk} \implies \delta_t = \sqrt{\delta_x^2 + \delta_y^2} \tag{27}$$

$$B = \text{square} \implies \delta_t = |\delta_x| + |\delta_y| \tag{28}$$

These nonlinear PDEs are satisfied at points where the data are smooth, i.e., the partial derivatives exist. However, even if the initial signal f is smooth, at finite scales $t > 0$ the above dilation or erosion evolution may create discontinuities in the derivatives, called *shocks*, which then continue propagating in scale-space. Thus, the multiscale dilations δ or erosions ε are *weak solutions* of the corresponding PDEs in the sense of [38]. Ways to deal with these shocks include replacing standard derivatives with morphological derivatives [12] or replacing the PDEs with differential inclusions [52]. For example, let

$$\mathcal{M}_x f(x,y) \triangleq \lim_{r \downarrow 0} \frac{\bigvee_{|v| \leq r} f(x+v, y) - f(x,y)}{r}$$

be the sup-derivative of f along the x-direction. If the right derivative $\partial_{x+} f$ and left derivative $\partial_{x-} f$ of f along the x-direction exist at point (x,y), then

$$\mathcal{M}_x f(x,y) = \max[0, \partial_{x+} f(x,y), -\partial_{x-} f(x,y)] \tag{29}$$

Similarly for the sup-derivative $\mathcal{M}_y f$ of f along the y-direction. Then, a generalized PDE generating flat dilations by a compact convex symmetric B is:

$$\frac{\partial \delta}{\partial t} = \sigma_B(\mathcal{M}_x \delta, \mathcal{M}_y \delta) \tag{30}$$

This new PDE can handle discontinuities (i.e., shocks) in the partial derivatives of δ provided that its left and right derivatives exist everywhere. However, the most acknowledged viewpoint for handling shocks and discontinuities is to use generalized solutions called *viscosity solutions* [19, 40].

The above PDEs for dilations/erosions of graylevel images by flat structuring elements directly apply to binary images, because flat dilations/erosions commute with thresholding and hence, when the graylevel image is dilated/eroded, each one of its thresholded versions representing a binary image is simultaneously dilated/eroded by the same element and at the same scale. However, this is not the case with graylevel structuring functions.

Next, we provide two examples of PDEs generating multiscale dilations by *graylevel structuring functions*. First, if we use the compact-support spherical function

$$k(x,y) = \begin{cases} \sqrt{1-x^2-y^2}, & x^2+y^2 \le 1 \\ -\infty, & x^2+y^2 > 1 \end{cases} \tag{31}$$

the dilation PDE becomes

$$\delta_t = \sqrt{1+(\delta_x)^2+(\delta_y)^2} \tag{32}$$

As shown in [12], this can be proven by using the semigroup structure of dilations and the first-order Taylor's approximation for the difference between dilations at scales t and $t+dt$. Alternatively, it can be proven using slope transforms, as explained next. As a second example of structuring function, if k is the infinite-support parabolic structuring function

$$k(x,y) = -r(x^2+y^2) \ \ , r > 0, \tag{33}$$

the dilation PDE becomes

$$\delta_t = [(\delta_x)^2 + (\delta_y)^2]/4r \tag{34}$$

This can be proven using slope transforms.

3.2 Slope Transforms and Dilation PDEs

All the above dilation (and erosion) PDEs can be unified using slope transforms. Specifically, let the unit-scale kernel $k(x,y)$ be a general upper-semicontinuous concave function, and consider its upper slope transform $K_\vee(\alpha_1,\alpha_2)$. Then, as discussed in [52, 29], the PDE generating multiscale signal dilations by k is

$$\frac{\partial \delta}{\partial t} = K_\vee\left(\frac{\partial \delta}{\partial x}, \frac{\partial \delta}{\partial y}\right) \tag{35}$$

Thus, the rate of change of δ in the scale (t) direction is equal to the upper slope transform of the structuring function evaluated at the spatial gradient of δ. Similarly, the PDE generating the multiscale erosion by k is:

$$\varepsilon_t = -K_\vee(\varepsilon_x, \varepsilon_y) \tag{36}$$

For example, the PDE (23) modeling the general flat dilation by a compact convex set B, i.e. by a flat function $k = \mathrm{I}_\vee(B)$, is a special case of (35) since the support function (24) of B is the upper slope transform of its $0/-\infty$ indicator function $\mathrm{I}_\vee(B)$; see Table 1. Likewise, the PDE (34) modeling multiscale dilations by parabolae results simply from (35) by noting that the upper slope transform of a concave parabola is a convex parabola. Similarly, Eq.(35) and Table 1 explain the spherical dilation PDE (32).

All the examined dilation and erosion PDEs are special cases of Hamilton-Jacobi equations, which are of paramount importance in physics. Such equations usually do not admit classic (i.e., everywhere differentiable) solutions but possess viscosity solutions [19]. Heijmans and Maragos [29] have shown via slope transforms that, the multiscale dilation by a general upper-semicontinuous concave function is the viscosity solution of the Hamilton-Jacobi dilation PDE (35).

3.3 Numerical Algorithm for Dilation PDEs

The PDEs generating flat dilation or erosion of f by disks are special cases of Hamilton-Jacobi PDEs of the type

$$\phi_t + \beta||\nabla\phi|| = 0 \tag{37}$$

with initial condition $\phi(x,y,0) = f(x,y)$, where $||\cdot||$ denotes Euclidean norm and β is the normal speed for moving the level sets of ϕ (as discussed in Section 4.) A constant speed equal to $\beta(x,y) = \pm 1$ yields dilation or erosion. Efficient algorithms for numerically solving (37) have been developed in [61] for curve evolution by adapting the technology of conservative monotone discretization schemes for shock-producing PDEs of hyperbolic conservation laws [38]. The goal is to compute an approximation $\Phi^n_{i,j}$ of the true solution values $\phi(i\Delta x, j\Delta y, n\Delta t)$ on a grid with spatial steps $\Delta x, \Delta y$ and time (scale) step Δt, given the initial values $\Phi^0_{i,j} = f(i\Delta x, j\Delta y)$ and the velocities $\beta_{ij} = \beta(i\Delta x, j\Delta y)$. Such a first-order algorithm replaces $\partial/\partial t$ with a forward difference and space derivatives with upwind combinations of finite differences

$$\begin{array}{lll} D_{+x}\Phi^n_{i,j} \triangleq \frac{\Phi^n_{i+1,j}-\Phi^n_{i,j}}{\Delta x} & , & D_{-x}\Phi^n_{i,j} \triangleq \frac{\Phi^n_{i,j}-\Phi^n_{i-1,j}}{\Delta x} \\ D_{+y}\Phi^n_{i,j} \triangleq \frac{\Phi^n_{i,j+1}-\Phi^n_{i,j}}{\Delta y} & , & D_{-y}\Phi^n_{i,j} \triangleq \frac{\Phi^n_{i,j}-\Phi^n_{i,j-1}}{\Delta y} \end{array}$$

and iterates the following:

$$\Phi^{n+1}_{i,j} = \Phi^n_{i,j} - \Delta t[(\beta_{ij} \vee 0)\nabla^+ + (\beta_{ij} \wedge 0)\nabla^-] \tag{38}$$

where $n = 0, 1, 2, ..., (T_{max}/\Delta t)$, T_{max} is the maximum time (or scale) of interest, and ∇^+, ∇^- are two different discretizations of the gradient magnitude required for positive and negative speed, respectively. One such discretization scheme was proposed in [61]:

$$\begin{array}{rcl} \nabla^+_{OS} & = & [\max(0, D_{-x})^2 + \min(0, D_{+x})^2 \\ & & + \max(0, D_{-y})^2 + \min(0, D_{+y})^2]^{1/2} \\ \nabla^-_{OS} & = & [\min(0, D_{-x})^2 + \max(0, D_{+x})^2 \\ & & + \min(0, D_{-y})^2 + \max(0, D_{+y})^2]^{1/2} \end{array} \tag{39}$$

where we use the abbreviations $D_{+x} = D_{+x}\Phi^n_{i,j}$. For *stability*, the space/time steps must satisfy $(\Delta t/\Delta x + \Delta t/\Delta y)\beta_{ij} \leq 0.5$.

An alternative discretization for the gradient magnitude results by replacing the partial derivative magnitudes $|\phi_x|, |\phi_y|$ in $||\nabla\phi||$ with the partial *morphological derivatives* $\mathcal{M}_x, \mathcal{M}_y$ from (29) and using the differences $D_{\pm x}, D_{\pm y}$ in place of the left/right derivatives required for $\mathcal{M}_x, \mathcal{M}_y$, as done in [12, 46]:

$$\begin{array}{rcl} \nabla^+_{MD} & = & [\max(0, D_{-x}, -D_{+x})^2 + \\ & & \max(0, D_{-y}, -D_{+y})^2]^{1/2} \\ \nabla^+_{MD} & = & [\min(0, D_{-x}, -D_{+x})^2 + \\ & & \min(0, D_{-y}, -D_{+y})^2]^{1/2} \end{array} \tag{40}$$

This $\mathcal{M}$-derivative discretization is less diffusive and faster than (39). It is actually equivalent to but slighty faster than the gradient discretization proposed in [68] for solving the eikonal PDE. It is also interesting that the direct discretization of morphological derivatives yields a monotone and consistent numerical approximation to the Hamiltonian $||\nabla\phi||$.

By choosing fine grids (and possibly higher-order terms) an arbitrarily low error (between signal values on the continuous plane and the discrete grid) can be achieved in implementing morphological operations involving disks as structuring elements. This is a significant advantage of the PDE approach, as observed in [4, 70]. Thus, curve evolution provides a geometrically better implementation of multiscale morphological operations with the disk-shaped structuring element. Figure 5 shows the results of a simulation to compare the traditional dilation of digital images via

discrete max-sum convolution of the image by digital approximations to disks, e.g., squares, versus a dilation which is the solution of the dilation PDE numerically solved using the algorithm (38). Comparing both the graylevel images and their binary versions (from thresholding at level=0) it is evident that the PDE approach to multiscale dilations can give much better approximations to Euclidean disks and hence avoid the abrupt shape discretization inherent in modeling digital multiscale dilations using discrete disks.

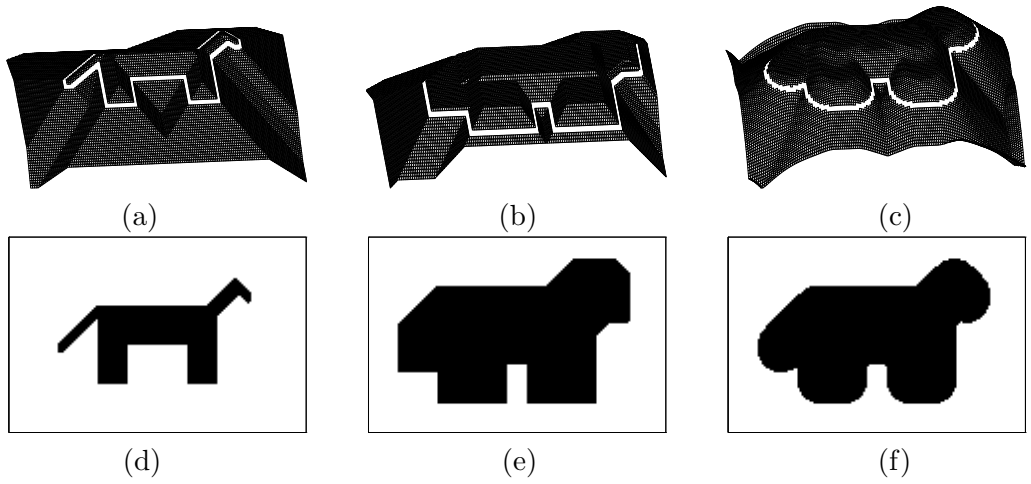

Figure 5: (a) Original digital gray-level image f and its contour at level=0. (b) Flat dilation $f \oplus B$ of f by a discrete disk, i.e. a square of $(2t+1) \times (2t+1)$ pixels with $t = 5$. (c) Dilation of f by a Euclidean disk at scale $t = 5$ by running the PDE $\partial\delta/\partial t = ||\nabla\delta||_2$ for $t \in [0, 5]$ with initial condition $\delta(x, y, 0) = f(x, y)$. (d) Binary image S from thresholding f at level=0. (e) Binary image $S \oplus B$ from thresholding $f \oplus B$ at level=0. (f) Binary image from thresholding the evolving image surface in (c) at level=0.

3.4 PDEs Generating Openings and Closings

Let $u(x, y, s) = [f(x, y) \ominus sB] \oplus sB$ be the multiscale flat opening of an image f by the disk B. This standard opening can be generated at some *fixed scale* $s > 0$ by running the following PDE [2]

$$u_t = \text{sgn}(t - s)||\nabla u|| \tag{41}$$

from time $t = 0$ until $t = 2s$ with initial condition $u(x, y, 0) = f(x, y)$, where $\text{sgn}(\cdot)$ denotes the signum function. This PDE has a time-dependent switching coefficient that make it act as an erosion PDE during $t \in [0, s]$ but as a dilation PDE during $t \in [s, 2s]$. At the switching instant $t = s$ this PDE exhibits discontinuities. This can be dealt with by making appropriate changes to the time scale that make time 'slow down' when approaching the discontinuity at $t = s$, as suggested in [2]. Of course, the solution u of the above PDE is an opening only at time $t = 2s$, whereas the solutions at other times is not a opening.

In a different work [12], a partial differential-difference equation was developed that models at *all* scales the evolutions of multiscale openings of 1D images by flat intervals. This does not involve only local operations but also global features such as the support geometry of peaks of f at various scales.

3.5 PDEs for Multiscale Reconstruction Filters

Reconstruction openings have found many more applications in a large variety of problems than the standard Minkowski openings. Levelings are a general class of morphological filters, which contain as special cases the reconstruction openings and closings [56]. They possess many interesting scale-space properties and are very efficient for image contour-preserving image simplification and

pre-segmentation. Next we present a nonlinear PDE, first introduced in [48] and then studied systematically in [46], that can generate reconstruction openings and closings. Consider a 2D *reference* signal $f(x,y)$ and a *marker* signal $m(x,y)$. If $m \leq f$ everywhere and we start iteratively growing m via incremental flat dilations with an infinitesimally small disk $\Delta t B$ but without ever growing the result above the graph of f, then in the limit we shall have produced the reconstruction opening of f (w.r.t. the marker m). The infinitesimal generator of this signal evolution can be modeled via a dilation PDE that has a mechanism to stop the growth whenever the intermediate result attempts to create a function larger than f. Specifically, let $u(x,y,t)$ represent the evolutions of f. Then, u is a weak solution of the PDE

$$\begin{cases} \partial u/\partial t &= -\text{sgn}(u-f)||\nabla u|| \\ u(x,y,0) &= m(x,y) \end{cases} \tag{42}$$

This PDE models a *conditional dilation* that grows the intermediate result as long as it does not exceed f. In the limit we obtain the final result $u_\infty(x,y) = \lim_{t\to\infty} u(x,y,t)$. The mapping $u_0 \mapsto u_\infty$ is the **reconstruction opening** filter. If in the PDE (42) we reverse the order between f and m, i.e., assume that $m \geq f$, then the positive growth (dilation) of m is replaced with negative growth (erosion) because now $\text{sgn}(f-u) \leq 0$. This negative growth stops when the intermediate result attempts to become smaller than f; in the limit we obtain the **reconstruction closing** of f with respect to the marker m.

What happens now if we use the PDE (42) when there is no specific order between f and m? In such a case, the PDE has a sign-varying coefficient $\text{sgn}(f-u)$ with spatio-temporal dependence which controls the instantaneous growth and stops it whenever $f = u$. The control mechanism is of a switching type: For each t, at points where $u < f$ it acts as a dilation PDE, whereas if $u > f$ it acts as an erosion PDE and reverses the direction of propagation. In [46] it was proved that this PDE has a steady-state $u_\infty(x) = \lim_{t\to\infty} u(x,t)$ which is the **leveling** of f with respect to $u_0 = m$, denoted by $u_\infty = \Lambda(m|f)$.

To solve the PDE (42) the following monotone and consistent numerical scheme was developed in [46]. Let $U_{i,j}^n$ be the approximation of $u(x,y,t)$ on a computational grid $(i\Delta x, j\Delta y, n\Delta t)$, with $U_{i,j}^0 = m(i\Delta x, j\Delta y)$, and $F_{i,j} = f(i\Delta x, j\Delta y))$. Then we solve the PDE (42) by iterating the following 2D nonlinear difference equation:

$$\begin{aligned} &U_{i,j}^{n+1} = \Phi(U_{i,j}^n), \quad n = 0,1,2,... \\ &\Phi(S_{i,j}) = [F_{i,j} \wedge \beta(S_{i,j})] \vee \alpha(S_{i,j}) \\ &\alpha(S_{i,j}) = S_{i,j} - \Delta t\ \nabla^+ S_{i,j} \\ &\beta(S_{i,j}) = S_{i,j} + \Delta t\ \nabla^- S_{i,j} \end{aligned} \tag{43}$$

where ∇^+ and ∇^- are the two discretizations in (40) of the gradient magnitude for positive and negative speed, respectively, based on morphological derivatives (29). By iterating the above for $n = 0,1,2,...$, we obtain in the limit a discrete leveling. For stability, $(\Delta t/\Delta x + \Delta t/\Delta y) \leq 0.5$ is required.

Consider a reference signal f and a leveling Λ. If we can produce various markers m_i, $i = 1,2,3,...$, that are related to some increasing scale parameter i, let us construct the levelings $g_i = \Lambda(m_i|g_{i-1})$, $i = 1,2,3,...$, with $g_0 = f$. The signals g_i constitute a hierarchy of *multiscale levelings* possessing the causality property that g_j is a leveling of g_i for $j > i$. One way to construct such multiscale levelings is to use a sequence of multiscale markers obtained from sampling a Gaussian scale-space. As shown in Fig. 6, the image edges and boundaries which have been blurred and shifted by the Gaussian scale-space are better preserved across scales by the multiscale levelings.

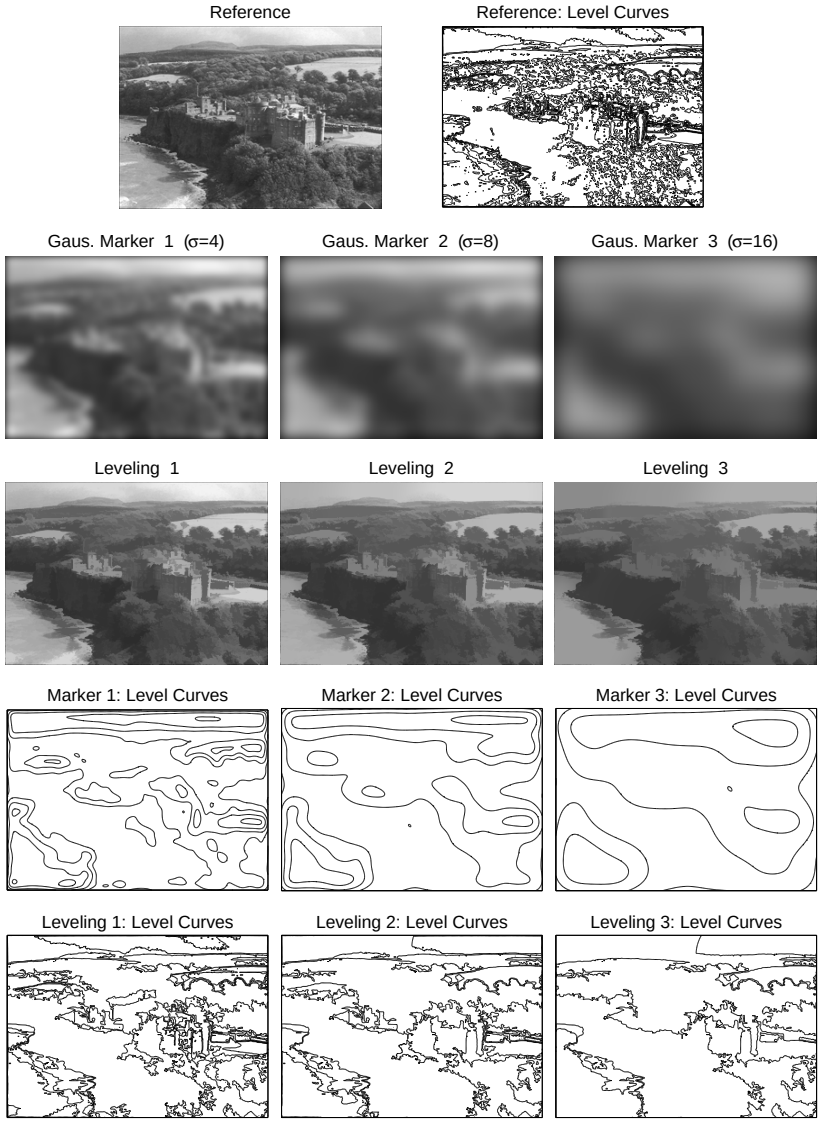

Figure 6: Multiscale image levelings $u(x, y, \infty)$ generated by the PDE $u_t = -\text{sgn}(u - f)||\nabla u||$. The markers $u(x, y, 0) = m(x, y)$ were obtained by convolving the original image with 2D Gaussians of standard deviations $\sigma_1 = 4$, $\sigma_2 = 8$, $\sigma_3 = 16$. At each scale σ_i as reference f was used the leveling of the previous scale σ_{i-1}. The last two rows show level curves of the markers and the corresponding levelings (6 level curves for each image).

4 Curve Evolution, Level Sets and Morphological Flows

Consider at time $t = 0$ an initial simple, smooth, closed planar curve $\Gamma(0)$ which is propagated for $t > 0$ along its normal vector field with speed V. Let $\Gamma(t)$ denote the set of points of this evolving curve (front). Consider also an analytic representation of the curve by its position vector $\vec{C}(s, t) = (x(s, t), y(s, t))$, parameterized by $s \in J$ so that it has its interior on the left in the direction of increasing s. The *curvature* along the curve is

$$\kappa = \kappa(s, t) \triangleq \frac{y_{ss}x_s - y_s x_{ss}}{(x_s^2 + y_s^2)^{3/2}} \tag{44}$$

The curve motion is governed by a general front propagation (flow)

$$\frac{\partial \vec{C}(s, t)}{\partial t} = V\vec{N}(s, t) \tag{45}$$

with initial condition $\Gamma(0) = \{\vec{C}(s,0) : s \in J\}$, where $\vec{N}(s,t)$ is the instantaneous unit *outward normal* vector at points on the evolving curve, and $V =< \vec{C}_t, \vec{N} >$ is the *normal speed*. This speed may generally depend on local geometrical information such as the curvature, global image properties, or other factors independent of the curve. The simplest speed is $V = 1$ or $V = -1$, in which case $\Gamma(t)$ is the boundary of the dilation or erosion of the initial curve $\Gamma(0)$ by a disk of radius t. A general speed model is

$$V = V_{dil} + V_{curv} + V_{adv} \tag{46}$$

The first velocity term $V_{dil} = \beta(x,y)$ models a propagation due to a dilation (expansion) or erosion (shrinkage), may be space-varying, and may depend on values of an underlying image or its gradient but not on curvature. The second velocity term V_{curv} is a function of curvature κ. The third term $V_{adv} =< \vec{F}, \vec{N} >$ exists if there is an advection of the moving curve due to an underlying vector field $\vec{F}$. Several special cases of (46) have been studied and applied extensively to image processing and computer vision problems modeled by curve evolution. Examples include: 1) the model $V = 1 - \epsilon\kappa$ studied in [61, 62, 74] for general evolution of interfaces and in [34] for shape analysis; 2) the case $V =$ constant for snake-type active contours as the 'balloon force' [18] and for isotropic multiscale morphology [4, 70]; 3) the case $V = -\kappa^{1/3}$ for affine-invariant scale-spaces [2, 71]; 4) all three terms of (46) (or their sub-combinations) for geometry-based active contours [15, 41, 85].

It is instructive to focus on the case $V = 1 - \epsilon\kappa$, with $\epsilon \geq 0$. As analyzed in [74], when $V = 1$ the front's curvature will develop singularities and the front will develop corners (i.e, the curve derivatives will develop shocks – discontinuities) at finite time if the initial curvature is anywhere negative. Two ways to continue the front beyond the corners are: i) If the front is viewed as a geometric curve, then each point is advanced along the normal by a distance t, and hence a 'swallowtail' is formed beyond the corners by allowing the front to pass through itself. ii) If the front is viewed as the boundary separating two regions, an *entropy condition* is imposed to disallow the front to pass through itself. Namely, if the front is a propagating flame, then 'once a particle is burnt it stays burnt' [74]. The same idea was also used in [9] to model grassfire propagation leading to the medial axis of a shape. It is equivalent to using Huygen's principle to construct the front as the set of points at distance t from the initial front. This can also be obtained from multiscale dilations of the initial front by disks of radii $t > 0$. Both the swallowtail and the entropy solutions are weak solutions. When $\epsilon > 0$, the curvature-dependent motion has a a nonlinear smoothing effect. Further, the limit of the solution for the $V = 1 - \epsilon\kappa$ case as $\epsilon \downarrow 0$ is the entropy solution for the $V = 1$ case [74]. In this case, the morphological set dilation picks the weak solution that satisfies the entropy condition.

4.1 Level Sets Formulation

To overcome the topological problem of splitting and merging and numerical problems with the Lagrangian formulation (45), an Eulerian formulation was proposed by Osher and Sethian [61] where the original curve $\Gamma(0)$ is first embedded in the surface of an arbitrary 2D Lipschitz continuous function $\phi_0(x,y)$ as its level curve (isoheight contour line) at constant level λ. For example, we can select $\phi_0(x,y)$ to be equal to the signed distance function from the boundary of $\Gamma(0)$, positive (negative) in the exterior (interior) of $\Gamma(0)$. Then, the evolving planar curve is embedded as constant-level curve of an evolving space-time function $\phi(x,y,t)$:

$$\begin{aligned} \Gamma(t) &= \{(x,y) : \phi(x,y,t) = \lambda\} \\ \Gamma(0) &= \{(x,y) : \phi_0(x,y) = \lambda\} \end{aligned} \tag{47}$$

We refer to ϕ as the *level function*. Without loss of generality, henceforth we set the constant level to $\lambda = 0$.

Geometrical properties of the evolving curve can be obtained from spatial derivatives of the level function. Thus, at any point on the front the curvature and outward normal of the level curves can be found from ϕ:

$$\vec{N} = \nabla\phi/||\nabla\phi||, \quad \kappa = \mathrm{div}(\nabla\phi/||\nabla\phi||) \tag{48}$$

The curve evolution PDE (45) induces a PDE generating its level function:

$$\left\{ \begin{array}{rcl} \partial\phi/\partial t & = & -V||\nabla\phi|| \\ \phi(x,y,0) & = & \phi_0(x,y) \end{array} \right. \tag{49}$$

If $V = 1$ or -1, by equating scale with time, the above function evolution PDE becomes identical to the PDE generating multiscale flat erosions or dilations by disks. Thus, we can view these specific morphological PDEs as special cases of the general function evolution PDE (49) where all level sets expand or shrink with unit normal speed. Curve evolution with a constant-sign space-varying $V = V(x,y)$ will lead us later to the eikonal PDE.

The function evolution PDE (49) makes all level curves $\{(x,y) : \phi(x,y,t) = \lambda\}$ of ϕ expand with normal speed V. Thus, differential curve evolution induces a similar differential evolution of a function whose level curves (at a constant level) are the evolving curves, and vice-versa. Let us view the evolution of the curve $\Gamma(t)$ to a new curve $\Gamma(t+\Delta t)$ at a later time as a set transformation Ψ, and the corresponding evolution of the level function ϕ as a function transformation ψ. Then, given that any (upper semicontinuous) function can be uniquely represented by its (closed) level sets $X_\lambda(f)$, which are the unions of the level curves and their interiors, it follows that the set operator Ψ induces a function operator ψ by operating on all level sets of an input function and vice-versa, as described by Eq.(8). This approach, of building function operators from set operators, and vice-versa, through level sets, has been extensively studied and used in morphological image analysis [73, 42, 28].

4.2 Numerical Algorithms

The success of the level sets formulation is largely due to the parallel development of efficient numerical algorithms for solving the function evolution PDE (49). For speeds V that are functions of position and not of curvature, the basic such first-order *level-set algorithm* is given by (38),(39) and was developed by Osher & Sethian [61]. If the speed is also a function of curvature and/or if higher-order approximations are needed, there are several similar numerical algorithms described in [61, 62, 74].

To reduce the computational complexity of the basic level-set numerical algorithm there are two main categories of fast numerical techniques, narrow banding and fast marching, described in [74, 62]. 1) *Narrow-Band Methods:* These apply to general speed functions V that can change sign and their idea is to track only a narrow band of pixels at the boundary of the evolving curve with a possible re-initialization of the level function ϕ over this band so that it corresponds to a signed distance function. 2) *Fast Marching Method (FMM):* This is a very fast algorithm that applies to constant-sign speeds $V(x,y) > 0$, in which case the initial-value PDE problem (49) becomes a boundary-value PDE problem of the eikonal type: $||\nabla T(x,y)|| = 1/V(x,y)$ where $T(x,y)$ is the first arrival time of the evolving curve at point (x,y).

4.3 Dilation Flows

In general, if B is a compact, convex, symmetric planar set of unit scale and if we dilate the initial curve $\Gamma(0)$ with tB and set the new curve $\Gamma(t)$ equal to the outward boundary of $\Gamma(0) \oplus tB$, then this action can also be generated by the following model [4, 70] of curve evolution

$$\frac{\partial \vec{C}}{\partial t} = \sigma_B(\vec{N})\vec{N} \tag{50}$$

Thus, the normal speed V, required to evolve curves by dilating them with B, is simply the support function of B evaluated at the curve's normal. Then, in this case the corresponding PDE (49) for evolving the level function becomes identical to the general PDE that generates multiscale flat erosions by B, which is given by (23) modulo a sign difference.

4.4 Curvature Flows

Another important case of curve evolution is when $V = -\kappa$; then,

$$\frac{\partial \vec{C}}{\partial t} = -\kappa \vec{N} = \frac{\partial^2 \vec{C}}{\partial \ell^2} \tag{51}$$

where ℓ is the arclength. This propagation model is known as *Euclidean geometric heat flow*, as well as *mean curvature motion*. According to some classic results in differential geometry, smooth simple curves, evolving by means of (51), remain smooth and simple while undergoing the fastest possible shrinking of their perimeter. Furthermore, any non-convex curve converges first to a convex curve and from there it shrinks to a round point.

If the function $\phi(x, y, t)$ embeds a curve evolving by means of (51), as its level curve at a constant level, then it satisfies the evolution PDE

$$\phi_t = \text{curv}(\phi)||\nabla \phi||$$

where $\text{curv}(\phi)$ is the curvature of the level curves of ϕ. This flow smooths all level curves by propagation under their mean curvature. It has many interesting properties and has been extensively studied by many researchers [61, 24, 17, 2, 27].

Solutions of the Euclidean geometric heat flow (51) are invariant with respect to the group of Euclidean transformations (rotations and translations). Extending this invariance to affine transformations creates the *affine geometric heat flow* introduced in [71]

$$\frac{\partial \vec{C}}{\partial t} = -\kappa^{1/3} \vec{N} = \frac{\partial^2 \vec{C}}{\partial \tau^2} \tag{52}$$

where τ is the affine arclength, i.e., a re-parameterization of the curve such that $\det[\vec{C}_\tau, \vec{C}_{\tau\tau}] = 1$. Any smooth simple non-convex curve evolving by the affine flow (52) converges to a convex one and from there to an elliptical point [71]. This PDE was also independently developed in [2] in the context of the affine morphological scale-space.

4.5 Morphological Representations of Curvature Flows

Matheron [51] proved that any set operator Ψ on $\mathcal{P}(\mathbb{R}^m)$ that is translation-invariant (TI) and increasing can be represented as the union of erosions by all sets of its kernel $\text{Ker}(\Psi) = \{X : 0 \in \Psi(X)\}$ as well as an intersection of dilations by all sets of the kernel of the dual operator:

$$\Psi(X) = \bigcup_{A \in \text{Ker}(\Psi)} X \ominus A, \quad X \subseteq \mathbb{R}^m.$$

This representation theory was extended by Maragos [42] to both function and set operators by using a basis for the kernel. According to the basis representation theory, every *TI, increasing*, and *upper-semicontinuous* (u.s.c.) operator can be represented as a supremum of morphological erosions by its basis functions. Specifically, let ψ be a signal operator acting on the set of extended-real-valued functions defined on $\mathbb{R}^m$ or $\mathbb{Z}^m$. If $\text{Ker}(\psi) = \{f : \psi(f)(0) \geq 0\}$ defines the *kernel* of ψ, then its *basis* $\text{Bas}(\psi)$ is defined as the collection of the minimal (w.r.t. $\leq$) kernel functions. Then [42]:

$$\psi(f) = \bigvee_{g \in \text{Bas}(\psi)} f \ominus g$$

This is a *sup-inf* representation of the operator ψ. Dually, ψ also admits an *inf-sup* representation, since it can be expressed as the infimum of dilations by the functions in the basis of its dual operator $\psi^*(f) = -\psi(-f)$.

If the above function operator ψ is also *flat* (i.e., binary inputs yield binary outputs), with Ψ being its corresponding set operator, and commutes with thresholding, i.e., $\forall \lambda$

$$X_\lambda[\psi(f)] = \Psi[X_\lambda(f)], \tag{53}$$

where $X_\lambda(f)$ are the upper level sets of f, then ψ is a supremum of flat erosions by the basis sets of its corresponding set operator Ψ [42]:

$$\psi(f) = \bigvee_{S \in \mathrm{Bas}(\Psi)} f \ominus S \tag{54}$$

where the basis $\mathrm{Bas}(\Psi)$ of the set operator Ψ is defined as the collection of its minimal kernel sets.

Condition (53) implies that the operator ψ is 'contrast-invariant', which means that $\psi(h(f)) = h(\psi(f))$, where $h : \mathbb{R} \to \mathbb{R}$ is any monotone bijective function. Such a function h is called an 'anamorphosis' in [73], or a 'contrast-change' in [1, 26].

The above morphological basis representations have been applied to various classes of operators, including morphological, median, stack, and linear filters [42]. Moreover, one can define TI, increasing and contrast-invariant filters as supremum (or infimum) of flat erosions (or dilations) by sets belonging to some arbitrary basis $\mathbb{B}$. Catté et al. [16] selected as a basis the scaled version of a unit-scale isotropic basis

$$\mathbb{B} = \{\text{all symmetric line segments of length 2}\}$$

and defined the following three types of multiscale flat operators $\mathcal{I}_t, \mathcal{S}_t, \mathcal{T}_t$:

$$\begin{aligned}
\mathcal{I}_t(f) &= \textstyle\bigvee_{S \in \mathbb{B}} f \ominus \sqrt{2t}S \Longleftrightarrow \vec{C}_t = -(\kappa \vee 0)\vec{N} \\
\mathcal{S}_t(f) &= \textstyle\bigwedge_{S \in \mathbb{B}} f \oplus \sqrt{2t}S \Longleftrightarrow \vec{C}_t = -(\kappa \wedge 0)\vec{N} \\
\mathcal{T}_t(f) &= [\mathcal{I}_{2t}(f) + \mathcal{S}_{2t}(f)]/2 \Longleftrightarrow \vec{C}_t = -\kappa\vec{N}
\end{aligned}$$

If these operators operate on a level function embedding a curve $\vec{C}$ as one of its level curves, then this curve evolves according to the above three flows. Hence, the above multiscale operators, which are sup-of-erosions and inf-of-dilations by linear segments in all directions, are actually curvature flows. A generalization of this result was obtained in [26], by assuming that $\mathbb{B}$ is any bounded and isotropic collection of planar sets. Furthermore, in different settings it has been shown that, by iterating n times a continuous median filter (implemented as a thresholded linear convolution), based on a window of scale s, we asymptotically converge (when $s \to 0$, $n \to \infty$, with $ns = t$) to the curvature flow. This idea and conjecture was originally proposed in [53] and then proven in [23, 7]. Relations between this iterated median filtering, morphological sup-inf representations, and curvature flows are discussed in [27, 14].

The above morphological representations deal with Euclidean curvature flow. In [26, 27] they were also extended to the affine curvature flow. Efficient implementations of the affine-invariant curve evolution and applications to shape smoothing are described in [57] and Chapter 4.15 of this book.

5 Distance Transforms

5.1 Distance Transforms and Wave Propagation

For binary images, the distance transform is a compact way to represent their multiscale dilations and erosions by convex polygonal structuring elements whose shape depends upon the norm used

to measure distances. For the applications herein, we view a subset S of the image domain as a source emanating a distance wave that propagates over its complement S^c. Thus, we define the *outer distance transform* of a set S w.r.t. the metric induced by some ℓ_p norm $||\cdot||_p$, $p = 1, 2, ..., \infty$, as the distance function

$$\mathrm{DT}_p(S)(x,y) \triangleq \bigwedge_{(v,w)\in S} ||(x-v, y-w)||_p \tag{55}$$

If we consider the $0/\infty$ indicator function of S

$$\mathrm{I}_\wedge(S)(x,y) \triangleq \begin{cases} 0, & (x,y) \in S \\ +\infty, & (x,y) \notin S \end{cases} \tag{56}$$

and the norm structuring function

$$g_p(x,y) = ||(x,y)||_p \tag{57}$$

it follows that the distance transform can be obtained from the infimal convolution of the indicator function of the set with the norm function:

$$\mathrm{DT}_p(S) = \mathrm{I}_\wedge(S) \oplus' g_p \tag{58}$$

If B_p is the unit ball induced by the norm $||\cdot||_p$, thresholding the distance transform at level $r > 0$ and obtaining the corresponding level set yields the morphological dilation of S by the ball B_p at scale r:

$$S \oplus rB_p = \{(x,y) : \mathrm{DT}_p(S)(x,y) \geq r\} \tag{59}$$

The boundaries of these dilations are the wavefronts of the distance propagation. Multiscale erosions of S can be obtained from the outer distance transform of S^c.

In addition to being a compact representation for multiscale erosions and dilations, the distance transform has found many applications in image analysis and computer vision. Examples include smoothing, skeletonization, size distributions, shape description, object detection and recognition, segmentation, and path finding [67, 9, 10, 81, 83, 65, 58, 77]. Thus, many algorithms have been developed for its computation.

Using Huygen's construction, the boundaries of multiscale erosions by disks can also be viewed as the wavefronts of a wave initiating from the original image boundary and propagating inwards with constant normal speed, i.e., in a homogeneous medium. Thus, the distance function has a minimum time-of-arrival interpretation [9] and its isolevel contours coincide with those of the wave phase function. Points where these wavefronts intersect and extinguish themselves (according to Blum's grassfire propagation principle) are the points of the skeleton (medial) axis of S [9]. Overall, the Euclidean distance function $\mathrm{DT}_2(S)$ is the weak solution of the following nonlinear PDE

$$\begin{cases} ||\nabla E(x,y)||_2 = 1, & (x,y) \in S^c \\ E(x,y) = 0, & (x,y) \in \partial S \end{cases} \tag{60}$$

This is a special case of the eikonal PDE, discussed later.

5.2 Euclidean Distance Transforms of Binary Images and Approximations

To obtain isotropic distance propagation, the Euclidean distance transform, i.e. using the norm $||\cdot||_2$ in Eq. (55), is desirable because it gives multiscale morphology with the disk as the structuring element. However, computing the Euclidean distance transform of discrete images has a significant computational complexity. Thus, various techniques are used to obtain approximate or the exact Euclidean distance transform at a lower complexity. Four types of approaches that deal with this problem are:

(1) Discrete metrics on grids that yield approximations to the Euclidean distance. Their early theory was developed in [67], based on sequential or parallel operations. This was followed later by a generalization in [10] based on *chamfer* metrics that yielded improved approximations.

(2) Fast algorithmic techniques that can obtain exact Euclidean distances by operating on complex data structures [20, 82].

(3) Infimal convolutions of binary images with a parabolic function yield the exact squared Euclidean distance transform [79, 32]:

$$[\mathrm{DT}_2(S)]^2 = \mathrm{I}_\wedge(S) \oplus' (g_2)^2 \tag{61}$$

The kernel in the above infimal convolution is a convex parabola $[g_2(x,y)]^2 = ||(x,y)||_2^2 = x^2+y^2$. Of course, convolution of the image with an infinite-extent kernel is not possible, and hence truncation of the parabola is used which incurs an approximation error.

(4) Efficient numerical algorithms for solving the nonlinear PDE (60) that yield arbitrarily close approximations to the Euclidean distance function.

Approach (4) yields the best approximations and will be discussed later. From the rest three approaches, (1) and (3) are more general than (2), have significant theoretical structure, and can be used with even the simplest data structures such as rectangularly or hegagonally-sampled image signals. Next we elaborate on approach (1) which is the most well-studied.

5.3 Chamfer Distance Transforms

The general chamfer distance transform is obtained by *propagating local distance steps* within a small neighborhood. For each such neighborhood the distance steps form a mask of weights that is infimally convolved with the image. For a 3×3-pixel neighborhood, if a and b are the horizontal and diagonal distance steps, respectively, the outer (a,b) chamfer distance transform of a planar set S can also be obtained directly from the general definition in Eq. (55) by replacing the general L_p norm $||\cdot||_p$ with the (a,b) **chamfer norm**

$$||(x,y)||_{a,b} \triangleq \max(|x|,|y|)a + \min(|x|,|y|)(b-a) \tag{62}$$

The unit ball corresponding to this chamfer norm is a symmetric octagon, and the resulting distance transform is

$$\mathrm{DT}_{a,b}(S)(x,y) = \bigwedge_{(v,w)\in S} ||(x-v, y-w)||_{a,b} \tag{63}$$

Note that the above two equations apply to sets S and points (x,y) both in the continuous plane $\mathbb{R}^2$ as well as in the discrete plane $\mathbb{Z}^2$.

For a 3×3-pixel neighborhood, the outer (a,b) chamfer distance transform of a discrete set $S \subseteq \mathbb{Z}^2$ can be obtained via the following sequential [67, 10] computation

$$\begin{aligned} u_n[i,j] \;=\; & \min\{\, u_{n-1}[i,j],\; u_n[i-1,j]+a, \\ & u_n[i,j-1]+a, u_n[i-1,j-1]+b, \\ & u_n[i+1,j-1]+b \,\} \end{aligned} \tag{64}$$

Starting from $u_0 = \mathrm{I}_\wedge(S)$ as the $0/\infty$ indicator function of S, two passes of the 2D recursive erosion (64) suffice to compute the outer chamfer distance transform of S if S^c is simply connected. *Forward pass:* During the first pass $(n=1)$ the image is scanned from top-left to bottom-right using the 4-point non-symmetric half-plane submask of the 3×3 neighborhood. *Backward pass:* During the second pass $(n=2)$ the image is scanned in the reverse direction using the reflected submask of distance steps. The final result $u_2[i,j]$ is the outer (a,b) chamfer distance transform of S evaluated at points of $\mathbb{Z}^2$. An example of the three images, u_0, u_1, and u_2, is shown in Fig. 7.

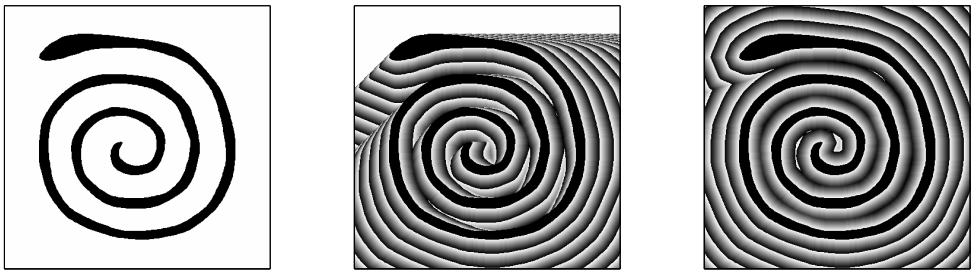

(a) (b) (c)

Figure 7: Sequential computation of the chamfer distance transform with optimal distance steps in a 3×3 mask. (a) Original binary image (b) Result after forward scan. (c) Final result after backward scan. (In (b) and (c) the distances are displayed as intensity values modulo a constant.)

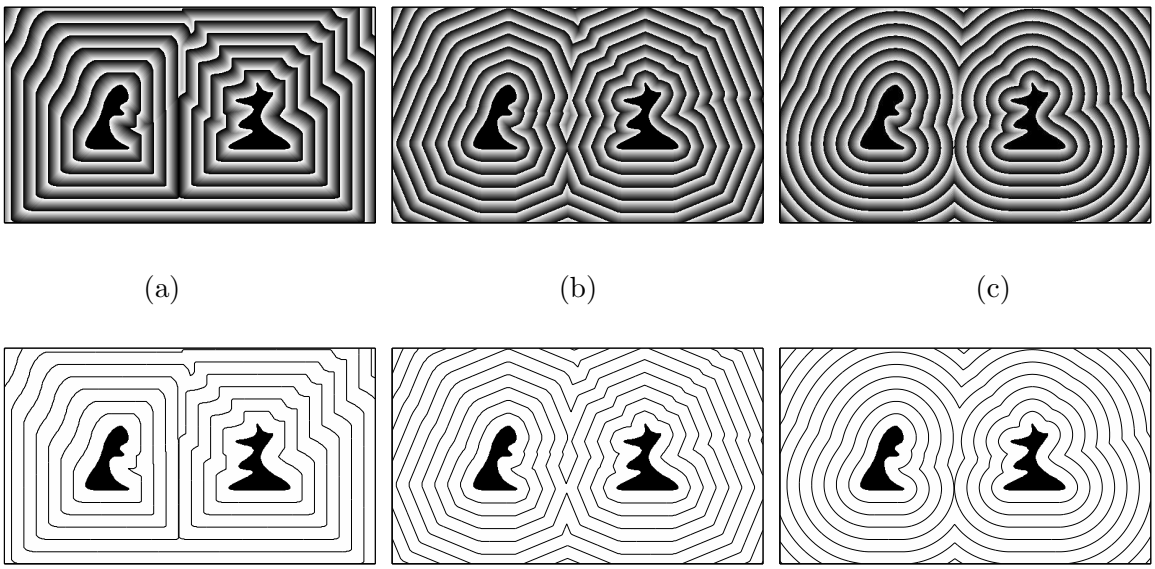

(a) (b) (c)

(d) (e) (f)

Figure 8: Distance transforms of a binary image obtained via: (a,) (1,1) chamfer metric; (b) optimal 3×3 chamfer metric; (c) eikonal PDE and curve evolution. In (a,b,c) the distances are displayed as intensities modulo a constant $h = 20$. Thresholding these three distance transforms at isolevel contours whose levels are multiples of h yields the multiscale dilations (at scales $t = nh$, $n = 1, 2, 3, ...$) of the original set (filled black regions) by various structuring elements: in (d,e) by the unit-scale polygons corresponding to the metrics used in (a,b), and in (f) by the disk. All images have resolution 450×600 pixels.

Selecting the steps a, b under certain constraints leads to an infinite variety of chamfer metrics based on a 3×3 mask. The two well-known and easily computable special cases of the cityblock metric with $(a, b) = (1, \infty)$ and the chessboard metric with $(a, b) = (1, 1)$ give the poorest discrete approximations to Euclidean distance (and to multiscale morphology with a disk structuring element) with errors reaching 41.4% and 29.3% respectively. Using Euclidean steps $(a, b) = (1, \sqrt{2})$ yields a 7.61% maximum error. Thus, a major design goal is to reduce the approximation error between the chamfer distances and the corresponding Euclidean distances [10]. A suitable error criterion is the maximum absolute error (MAE) between a unit chamfer ball and the corresponding unit disk. The optimal steps obtained in [13] by minimizing this MAE are $a = 0.9619$ and $b = 1.3604$, which give a 3.957% maximum error. In practice, for faster implementation, integer-valued distance steps are used, and the computed distances are divided by a normalizing constant.

An optimal pair from [13] is $(a, b) = (70, 99)/72.77$ yielding a 3.959% MAE. See Fig. 8 for an example. Optimal steps can also be found for chamfer distances with a 5×5 or larger neighborhood that yield an even lower error.

5.4 Distance Transforms as Slope Filters

By Eq. (58), the L_p-distance transform of S can be obtained from the infimal convolution of the set's indicator function $\mathrm{I}_\wedge(S)$ with the norm function $g_p(x, y) = ||(x, y)||_p$. By Table 1, this is equivalent to passing the input signal, i.e., the set's indicator function, through an ETI system with lower slope response

$$G_\wedge(\alpha) = \begin{cases} 0, & ||\alpha||_q \le 1 \\ -\infty, & ||\alpha||_q > 1 \end{cases} \tag{65}$$

where q is the conjugate exponent of p $(1/p + 1/q = 1)$. That is, the distance transform is the output of an ideal-cutoff slope-selective filter that rejects all input planes whose slope vector falls outside the unit ball with respect to the $||\cdot||_q$ norm, and passes all the rest unchanged.

For example, consider the (a, b) chamfer distance trasform, implemented by iterating the recursive min-sum difference equations (64). As explained in [45], each such iteration and their combinations correspond to ETI systems with infinite impulse responses and binary slope responses. Specifically, the forward pass mapping $u_0 \mapsto u_1$ is an ETI system with an infinite impulse response (found via induction)

$$g_f[i, j] = \begin{cases} ||(i, j)||_{a,b}, & i + j \ge 0,\ j \ge 0 \\ +\infty, & \text{else} \end{cases} \tag{66}$$

The slope response $G_f(\alpha)$ of this ETI system is equal to the $0/-\infty$ indicator function of the region shown in Fig. 9(a). The backward pass mapping $u_1 \mapsto u_2$ is an ETI system with an infinite impulse response $g_b[i, j] = g_f[-i, -j]$ and with a slope response $G_b(\alpha) = G_f(-\alpha)$. The final chamfer distance transform mapping $u_0 \mapsto u_2$ is an ETI system with an infinite impulse response $g = g_f \oplus' g_b$, which equals the chamfer norm $g[i, j] = ||(i, j)||_{a,b}$. Infimal convolution corresponds to addition of lower slope transforms; hence the overall slope response is $G(\alpha) = G_f(\alpha) +' G_f(-\alpha)$ and equals the $0/-\infty$ indicator function of the octagon region shown Fig. 9(b). Thus, using ETI systems theory it can be shown that, both in space and slope domain, the two-pass computation via the recursive min-sum difference equations (64) whose coefficients are the local distances yields the chamfer distance transform.

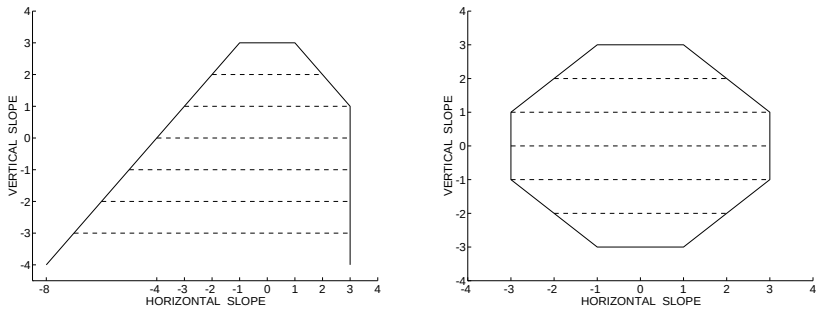

(a) (b)

Figure 9: Regions of support of binary slope responses of discrete ETI systems representing: (a) the forward pass of the chamfer (3,4) distance transform. (b) the chamfer (3,4) distance transform.

The distance propagation can also be implemented in paralell via non-recursive min-sum equations, which correspond to ETI systems with finite impulse responses, as explained in [45].

Examples: The *cityblock* distance transform is obtained using $a = 1$ and $b = +\infty$, i.e., using the 5-pixel rhombus as the unit 'disk'. It is an ETI system with impulse response $g[i, j] = |i| + |j|$ and

slope response the indicator function of the unit square $\{\alpha : ||\alpha||_\infty = 1\}$. Similarly, the *chessboard* distance transform is obtained using $a = b = 1$. It is an ETI system with impulse response $g[i,j] = \max(|i|, |j|)$ and slope response the indicator function of the unit rhombus $\{\alpha : ||\alpha||_1 = 1\}$.

6 Eikonal PDE and Distance Propagation

6.1 Eikonal

Let us assume a planar medium with bounded connected domain $\Omega \subseteq \mathbb{R}^2$ where light propagates with (possibly space-varying) speed $\beta(x,y)$; let $\eta(x,y) = c_0/\beta(x,y)$ be its refractive index, where c_0 is the speed of light in free space. In such a medium consider two points $A = (x_1, y_1)$ and $B = (x_2, y_2)$ connected by a piecewise-smooth path $\gamma(\ell)$ parameterized by arclength ℓ. If light were to travel along this path, this would take time equal to $T_\gamma = W(\gamma)/c_0$ where $W(\gamma) = \int_\gamma \eta(\gamma(\ell))d\ell$ is the *weighted* path length. The main postulate of geometrical optics is Fermat's *principle of least time*, which states that light will choose a path between A and B that minimizes the weighted path length. The minimum weighted length, called **optical path length**, is equal to

$$L(A,B) \triangleq \inf_{\gamma \in [A \rightsquigarrow B]} \int_0^{\mathrm{Len}(\gamma)} \eta(\gamma(\ell))d\ell \tag{67}$$

where $[A \rightsquigarrow B]$ denotes the set of all paths γ between A and B and $\mathrm{Len}(\gamma)$ denotes the Euclidean length of γ. The optimal paths, called *rays*, are the light trajectories. An alternative viewpoint of geometrical optics is to consider the scalar function $E(x,y)$, called the **eikonal**, whose (isoheight) level curves are everywhere normal to the rays. Thus the eikonal's gradient ∇E is parallel to the rays. Fermat's principle in optics is equivalent to the following PDE

$$||\nabla E(x,y)|| = \sqrt{(E_x)^2 + (E_y)^2} = \eta(x,y) \tag{68}$$

called the *eikonal equation*. By integrating the eikonal equation along a light ray γ^* between two points A and B we obtain

$$\begin{array}{rcl} E(B) - E(A) & = & \int_0^{\mathrm{Len}(\gamma^*)} ||\nabla E(\gamma^*(\ell))||d\ell \\ & = & L(A,B) \end{array} \tag{69}$$

Thus, the eikonal difference $E(B) - E(A)$, in analogy to the potential difference in electrostatics, gives us the optical path length between A and B which is proportional to the minimum time required for the light propagation.

A formal solution of the eikonal PDE was given by Lions [40] using viscosity solutions of Hamilton-Jabobi equations. Assume that we are given over a bounded smooth connected domain $\Omega \subseteq \mathbb{R}^2$ the continuous scalar field $\eta(x,y) \geq 0$ which is positive except at some point[4] sources m_i, $i = 1, ..., K$:

$$\eta(p) > 0 \quad \forall p \in \overline{\Omega} \setminus \{m_1, ..., m_K\}, \quad \eta(m_i) = 0 \ \ \forall i. \tag{70}$$

Consider the boundary-value PDE problem

$$\left\{ \begin{array}{rcll} ||\nabla E(x,y)|| & = & \eta(x,y) & \text{in} \quad \Omega \\ E(x,y) & = & 0 & \text{on} \quad \partial\Omega \end{array} \right. \tag{71}$$

Then, as shown in [40, 68], a viscosity solution of (71) satisfying the boundary conditions[5]

$$E(m_i) = h_i, \quad i = 1, 2, ..., K \tag{72}$$

[4]The solution of (71) can be extended to the case where the sources are compact subsets of $\overline{\Omega}$ over which η is zero.

[5]The boundary values h_i at the sources must satisfy certain compatibility conditions [40, 68].

is given at each point $p = (x, y)$ of $\overline{\Omega}$ by

$$E(p) = \bigwedge_{i=1}^{K} \{L(m_i, p) + h_i\} \tag{73}$$

Note the significance of the optical path length function L, which is continuous and a semi-metric. Further, the above solution can be viewed as the value function of an optimal control problem using the dynamic programming principle, and this interpretation is useful for developing efficient numerical algorithms [68, 78].

6.2 Arrival Time and Level Sets

In the above settings of the eikonal problem with all $h_i = 0$, assume an optical wave propagating in the 2D medium Ω at wavelengths much smaller than the image objects, so that ray optics can approximate wave optics. Then, the eikonal E of ray optics is proportional to the phase of the wavefunction. Hence, the level curves of E are the *wavefronts*. Assume that the wave sources are compact subsets $M_i \subseteq \Omega$, $i = 1, ..., K$, and at time $t = 0$ the wave starts propagating outward from the source set $S = \bigcup_i M_i$ with speed $\beta(x, y) = c_0/\eta(x, y)$.

If $\Gamma(t)$ denotes the set of points of the zero-phase wavefront at time t, then we can model the propagation as a curve evolution with normal speed $\beta(x, y)$ starting at $t = 0$ from the initial wavefront $\Gamma(0) = \partial S$, i.e. the source boundary. Note that we can trace this wavefront propagation using Huygen's *envelope construction*: Namely, if we dilate the points (x, y) of the wavefront curve at a certain time t with circles of infinitesimal radius $\beta(x, y)dt$, the envelope of these circles yields the wavefront at time $t + dt$. If $T(x, y)$ is the minimum time required for the wavefront to arrive at any point $(x, y) \in \Omega$ from the sources, then $E(x, y) = c_0 T(x, y)$. Thus, the **arrival time** function T is solution of the following eikonal PDE:

$$\begin{cases} ||\nabla T(x,y)|| &= 1/\beta(x,y) \quad \text{in} \quad \Omega \\ T(x,y) &= 0 \qquad\quad\ \ \text{on} \quad \Omega \setminus S \end{cases} \tag{74}$$

Now, by modeling curve evolution with level sets, we can also embed the propagating zero-phase wavefront $\Gamma(t)$ as the zero-level curve of a function $\phi(x, y, t)$, where $\phi(x, y, 0) = \phi_0(x, y)$ is the signed (positive in the curve exterior and negative in the interior) distance from $\Gamma(0)$. Namely,

$$\begin{aligned} T(x,y) &= \inf\{t : \phi(x,y,t) = 0\} \\ \phi_0(x,y) &= \text{signed distance of } S \end{aligned} \tag{75}$$

Then, the embedding function ϕ evolves according to the PDE

$$\frac{\partial \phi}{\partial t} = -\beta(x, y)||\nabla \phi|| \tag{76}$$

By solving this PDE, $T(x, y)$ can be found as the minimum time at which the zero-level curve of $\phi(x, y, t)$ crosses (x, y).

6.3 Numerical Algorithms for Eikonal

The solution $E(x, y)$ of the eikonal PDE is a *weighted distance transform (WDT)* whose values at each pixel give the minimum distance from the light sources weighted by the gray values of the refractive index field. On a computational grid this solution is numerically approximated using discrete WDTs which can be implemented either via 2D recursive min-sum difference equations or via numerical algorithms of curve evolution. The former implementation employs adaptive 2D recursive erosions, whereas the latter evolves curves based on a dilation-type PDE with speed varying according to the gray values. Next we outline these two ways of solving the eikonal PDE and discuss some of its applications.

6.3.1 WDT based on Chamfer Metrics

Let $f[i,j] \geq 1$ be a sampled nonnegative graylevel image and let us view it as a discrete refractive index field. Also let S be the set of 'sources' of some wave or the location of the wavefront at time $t = 0$. The discrete WDT finds at each pixel $[i,j]$ the smallest sum of values of f over all possible discrete paths connecting this pixel to the sources. It can also be viewed as a procedure of finding paths of minimal 'cost' among nodes of a weighted graph or as discrete dynamic programming. It has been used extensively in image analysis problems such as minimal path finding, weighted distance propagation, and graylevel image skeletonization [39, 81].

The above discrete WDT can be computed by running a 2D min-sum difference equation like Eq. (64) that implements the chamfer distance transform of binary images but with space-varying coefficients proportional to the gray image values [81]:

$$\begin{aligned} u_n[i,j] = \quad \min\{\ & u_{n-1}[i,j],\ u_n[i-1,j] + af[i,j], \\ & u_n[i,j-1] + af[i,j], \\ & u_n[i-1,j-1] + bf[i,j], \\ & u_n[i+1,j-1] + bf[i,j]\ \} \end{aligned} \tag{77}$$

where $u_0 = \mathrm{I}_\wedge(S)$ is the $0/\infty$ indicator function of the source set S. Starting from u_0, a sequence of functions u_n is iteratively computed by running Eq. (77) over the image domain in a forward scan for even n, whereas for odd n an equation as in (77) but with a reflected coefficient mask is run in a backward scan. In the limit $n \to \infty$ the final WDT u_∞ is obtained. In practice, this limit is reached after a finite number of passes. The number of iterations required for convergence depends on both the sources and the gray values. There are also other faster implementations using queues [81, 54]. The final transform is a function of the source set S, the index field f and the chamfer norm used for horizontal distances.

The above WDT based on discrete chamfer metrics is a discrete approximate solution of the eikonal PDE. The rationale for such a solution is that, away from the sources, this difference equation mapping $f \mapsto u$ corresponds to

$$\bigvee_{(k,\ell)\in B} \frac{u[i,j] - u[i-k, j-\ell]}{a_{ij}} = f[i,j] \tag{78}$$

where B is equal to the union of the output mask and its reflection and a_{ij} are the chamfer steps inside B. Comparing the left side of Eq. (78) with (1) shows that the former is a weighted discrete approximation to the morphological derivative $\mathcal{M}(-u)$ where horizontal distances are weighted by a_{ij}. Thus, since in the continuous differentiable case $\mathcal{M}(-u) = ||\nabla u||$, Eq. (78) is an approximation of the eikonal.

To improve the WDT approximation to the eikonal's solution, one can optimize (a,b) so that the error is minimized between the planar chamfer distances and Euclidean distances. Using a neighborhood larger than 5×5 can further reduce the approximation error but at the cost of an even slower implementation. However, for WDT-based image segmentation, larger neighborhood masks give erroneous results and hence cannot be used because they can bridge over a thin line that separates two segmentation regions. Overall, the chamfer metric approach to WDT is fast and easy to implement, but due to the required small neighborhoods is not isotropic and cannot achieve high accuracy.

6.3.2 WDT based on Curve Evolution

In this approach, at time $t = 0$ the boundary of the sources' set is modeled as a curve $\Gamma(0)$ which is then propagated with normal speed $\beta(x,y) = c_0/\eta(x,y)$. The propagating curve $\Gamma(t)$ is embedded as the zero-level curve of a function $\phi(x,y,t)$, which evolves according to the PDE $\phi_t = -\beta||\nabla\phi||$.

The value of the resulting WDT at any pixel (x, y) of the image is the time it takes for the evolving curve to reach this pixel, i.e., the smallest t such that $\phi(x, y, t) \geq 0$. This is an initial-value problem formulation of the eikonal PDE. It can be solved via the basic level-set tracking numerical algorithm (38). This continuous approach to WDT can achieve sub-pixel accuracy, as investigated in [36]. In the applications of the eikonal PDE examined herein, the speed function $\beta(x, y)$ is everywhere nonnegative. In such cases the computational complexity of the basic level-set algorithm (which can handle sign changes in the speed function) can be significantly reduced by solving the corresponding boundary-value formulation of the eikonal PDE, i.e., $||\nabla T|| = 1/\beta$, which does not involve a time evolution. There exist several efficient *iterative* numerical algorithms to solve this stationary eikonal equation; examples include [6, 25, 68]. However, the currently fastest algorithm is the *fast marching method (FMM)* [74].

The image experiments shown herein that compare chamfer-based versus curve evolution WDTs have been produced using an implementation of fast marching based on a simple data structure of two queues. This is explained in [47] and has been used to implement WDTs based either on chamfer metrics or on fast marching, for applications both with single sources as well as with multiple sources where triple points develop at the collision of several wavefronts.

7 Applications of Eikonal PDE

Many tasks for extracting information from images have been related to optics and wave propagation via the eikonal PDE. Its solution $E(x, y)$ can provide Euclidean distance transforms, shape from shading, contour-based image halftoning, and topographic segmentation of an image by choosing the refractive index field $\eta(x, y)$ to be an appropriate function of the image brightness [72, 31, 81, 64, 59, 36]. In the next applications fast marching [74] has been used for numerically solving the eikonal PDE.

7.1 Euclidean Distance Transform

Given a source set S, by choosing $\eta(x, y)$ to be the binary indicator function of S^c, the solution of the eikonal problem (60) yields the Euclidean distance transform of S. As shown in Fig.8, the curve evolution approach yields an almost ideal approximation to the true Euclidean distances and is superior to the chamfer metrics. Comparisons and fast algorithms are discussed in [47].

7.2 Gridless Halftoning

Schröder [72] proposed the use of the eikonal function's contour lines for visually perceiving an intensity image $I(x, y)$. Inspired by this work, Verbeek & Verwer [81] and especially Pnueli & Bruckstein [64] proposed various numerical schemes to solve the PDE

$$||\nabla E(x, y)|| = \text{constant} - I(x, y) \tag{79}$$

and create a binary *gridless* halftone version of $I(x, y)$ as the union of the level curves of the eikonal function $E(x, y)$. The larger the intensity value $I(x, y)$, the smaller the local density of these contour lines in the vicinity of (x, y). This eikonal PDE approach to gridless halftoning, which we call *eikonal halftoning*, is indeed very promising and can simulate various artistic effects, as shown in Fig. 10. There we also see that the curve evolution WDT gives a smoother halftoning of the image than the WDTs based on chamfer metrics.

7.3 Shape-from-Shading

An important 3D reconstruction problem in computer vision is *shape-from-shading*. Its goal is to find the height function $Z(x, y)$ of the surface of a 3D object whose illumination yields a 2D image

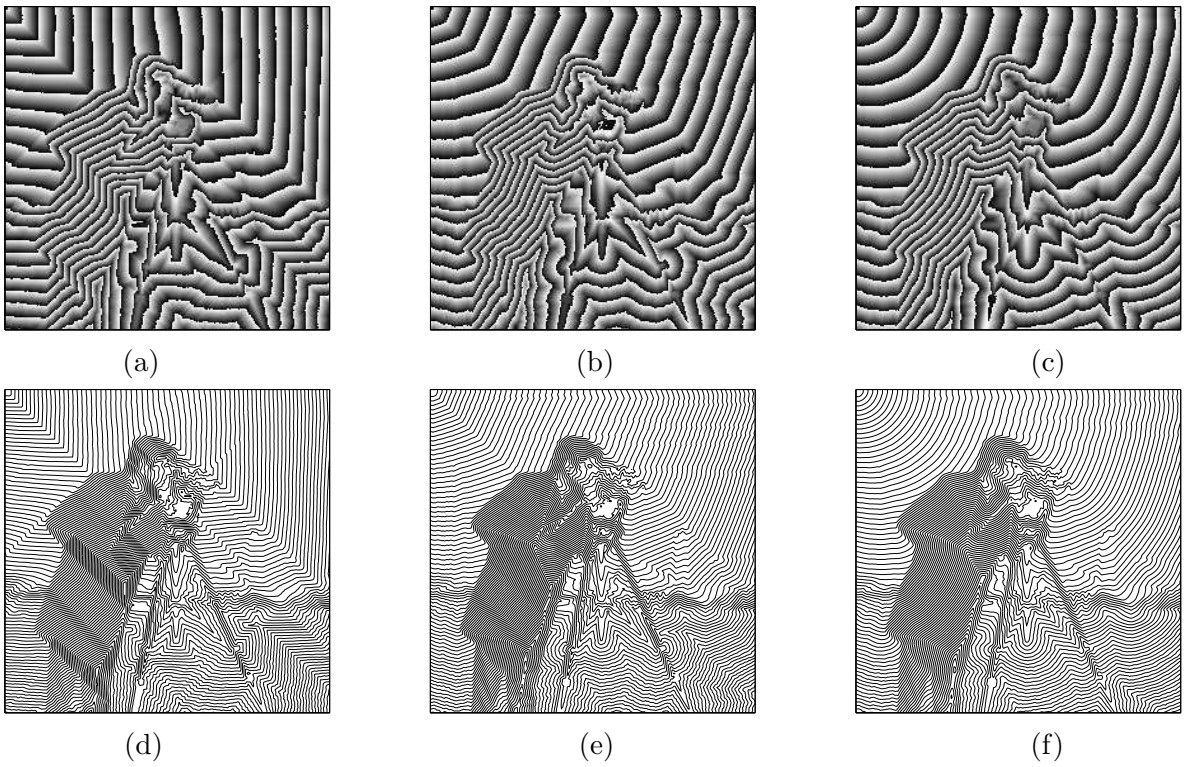

Figure 10: Eikonal halftoning of the CAMERAMAN image I from the weighted distance transform (WDT) of the 'negative' image $\max(I) - I$. In (a,b,c) the light source was at the top left corner, and the WDTs (displayed as intensities modulo a height such that 25 waves exist per image) were obtained via: (a) (1,1) chamfer metric; (b) optimal 3×3 chamfer metric; (c) curve evolution. In (d,e,f) 100 contour lines of the WDTs in (a,b,c), respectively, give a gridless halftoning of the original image.

matching a given intensity image $I(x, y)$, if the illumination source location and surface reflectivity are known. Assuming a Lambertian surface illuminated vertically, the unknown function Z satisfies the following eikonal PDE [31, 81, 68]

$$||\nabla Z(x, y)|| = \sqrt{1/I^2(x, y) - 1} \tag{80}$$

Numerical solutions to the eikonal, or equivalently to finding weighted distance transforms, solving shape from shading problems have been developed in [81] using discrete weighted distance algorithms implemented via queues, in [68] using numerical schemes like (40) inspired by dynamic programming, and in [36, 35] using curve evolution implemented via level set algorithms.

7.4 Watershed Segmentation

Segmentation is one of the most important and difficult tasks in image analysis. A powerful morphological approach to image segmentation is the *watershed* [8, 83] which transforms an image $f(x, y)$ to the crest lines separating adjacent catchment basins that surround regional minima or other 'marker' sets of feature points. The segmentation process starts with creating flooding waves that emanate from the set of markers and flood the image gradient surface. The points where the emanating waves meet each other form the segmentation boundaries. Very fast algorithms to find a digital watershed via flooding have been developed based on immersion simulations [83] and hierarchical queues [8]. The simplest markers are the regional minima of the gradient image, but very often they are extremely numerous and lead to oversegmentation. Thus, in practice the flooding sources are a smaller set of markers, which have been identified by a preliminary step as inside particles of the regions or objects that need to be extracted via segmentation. The robust

watershed version using *markers* has been successfully used for both interactive and automated segmentation.

There is also an eikonal interpretation of the watershed. Najman & Schmitt [59] have established that (in the continuous domain and assuming that the image is sufficiently smooth and has isolated critical points) the continuous watershed is equivalent to finding a skeleton by influence zones with respect to a weighted distance function that uses points in the regional minima of the image f as sources and $||\nabla f||$ as the field of indices. A similar result has been obtained by Meyer [54] for digital images. In Maragos and Butt [47] the eikonal PDE modeling the watershed segmentation of an image-related function f has been solved by finding a WDT via level sets and curve evolution where the curve's normal speed is proportional to $1/||\nabla f||$. Specifically, if $\vec{C}$ is a curve representing a marker boundary, then the propagation of the corresponding flooding wave is modeled by

$$\frac{\partial \vec{C}}{\partial t} = V\vec{N}, \quad V = \frac{c_0}{||\nabla f||} \tag{81}$$

Thus the curve speed is proportional to $1/||\nabla f||$. Related ideas can be found in [76]. Subsequently, Nguyen et al. [60] proposed a PDE segmentation approach that combines the watershed ideas with active contours. Namely, they used curve evolution as in (81) but with a velocity $V = c_0/||\nabla f|| - c_1\kappa$ that contains both the eikonal speed $1/||\nabla f||$ and a term proportional to curvature that smoothens the evolving boundaries. Further, they related this combined curve evolution to minimizing an energy functional.

The stationary eikonal PDE $||\nabla T|| = 1/V$ corresponding to (81), where T is the curve's arrival time, was solved in [47] using the FMM. Further, the results of this eikonal PDE segmentation approach were compared to the digital watershed algorithm via flooding [83] and to the eikonal approach solved via a discrete chamfer WDT [81, 54]. In all three approaches, robust features are extracted first as markers of the regions, and the original image I is transformed to another function f by smoothing via alternating opening-closings, taking the gradient magnitude of the filtered image, and changing (via morphological reconstruction) the homotopy of the gradient image so that its only minima occur at the markers. The segmentation is done on the final outcome f of the above processing.

In the standard digital watershed algorithm [83, 8], the flooding at each height level is achieved by a planar distance propagation that uses the chess-board metric. This kind of distance propagation is not isotropic and could give wrong results, particularly for images with large plateaus. Eikonal segmentation using chamfer WDTs improves this situation a little but not entirely. In contrast, for images with large plateaus/regions, segmentation via the eikonal PDE and curve evolution WDT gives results close to ideal. As Fig. 11 shows, compared on a test image that is difficult (because expanding wavefronts meet watershed lines at many angles ranging from being perpendicular to almost parallel), the continuous segmentation approach based on the eikonal PDE and curve evolution outperforms the discrete segmentation results [47].

The standard watershed flooding, both in the digital algorithms [8, 83] as well as in the eikonal curve evolution (81), corresponds to a uniform *height flooding*. This height criterion corresponds to a contrast-based segmentation. Alternative criteria, such as area (size-based segmentation) or volume (contrast and size-based segmentation) and corresponding generalized floodings have been considered in [55]. In [75] the uniform *volume flooding* was modeled via a time-dependent eikonal-type PDE and level sets. In this new model the evolution of a marker's boundary curve $\vec{C}$ is described by

$$\frac{\partial \vec{C}}{\partial t} = V\vec{N}, \quad V(x,y,t) = \frac{c_0}{A(t)||\nabla f(x,y)||} \tag{82}$$

where $A(t)$ denotes the instant area enclosed by the evolving curve. The corresponding stationary eikonal PDE is

$$||\nabla T(x,y)|| = A(T)||\nabla f(x,y)||/c_0 \tag{83}$$

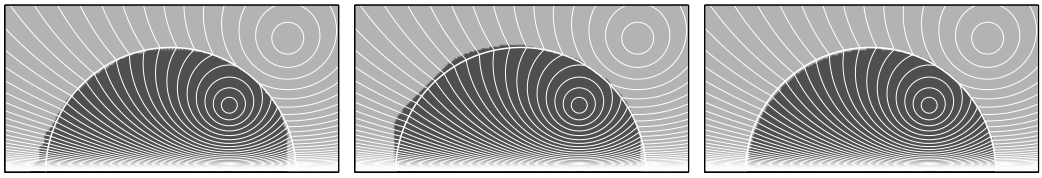

(a) (b) (c)

Figure 11: Performance of various segmentation algorithms on a TEST image (250×400 pixels). This image is the minimum of two potential functions. Its contour plot (thin bright curves) is superimposed on all segmentation results. Markers are the two source points of the potential functions. Segmentation results based on: (a) Digital watershed flooding algorithm. (b) WDT based on optimal 3×3 chamfer metric. (c) WDT based on curve evolution (the thick bright curve shows the correct segmentation).

where T is arrival time. Whereas in the case of uniform height flooding the FMM-based solution of the eikonal PDE was simple to implement as done in [47], in the case of uniform volume flooding solving the stationary PDE (83) has the peculiarity of the time-varying term $A(T)$. This was numerically solved in [75] using a variation of the FMM that took into consideration the time-dependent area variations of the fronts.

Experimental results of the PDE-based height and volume flooding applied to real image segmentation are shown in Fig.12. The volume flooding seems to perform in a more balanced way. This is expected since it exploits both the contrast and the (area) size properties of the objects-regions present in an image. It is a useful segmentation tool in cases where we want to keep a balance between the aforementioned image properties and can give good results in cases that contrast-based driven segmentation fails. In addition, the PDE implementation has the advantage of a more isotropic flooding.

8 Conclusions

In this chapter we have presented some basic results from the theory, algorithms and applications of 1) nonlinear geometric PDEs that can generate multiscale morphological operators, 2) the eikonal PDE that can model weighted distance propagation, and 3) slope transforms to analyze morphological PDEs and distance transforms in a slope domain. Also related to these is 4) the area of curve evolution and level set methods. The PDEs governing multiscale morphology, the eikonal and some cases of curve evolution via level sets are of the Hamilton-Jacobi type.

We view the intersection of the above related themes as a unified area in nonlinear image processing which we call *differential morphology*, and we have briefly discussed some of its potential applications to image processing.

Interpreting and modeling the morphological operators and distance transforms via PDEs has several advantages, mathematical, physical, and computational. Further, it opens up several new promising directions along which mathematical morphology can both assist and be assisted by other PDE-based theories and methodologies of image analysis and computer vision, with a broad spectrum of applications.

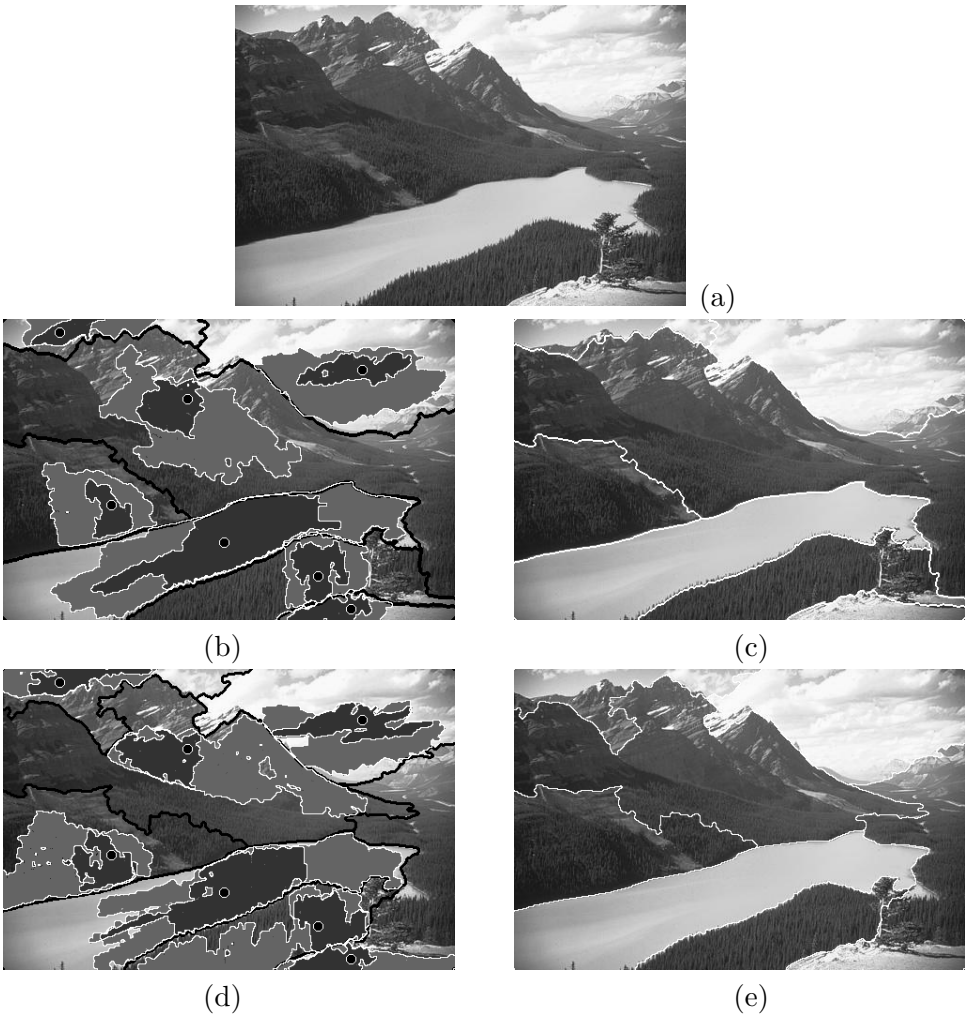

Figure 12: Watershed-type segmentation with various PDE-based floodings. (a) Original image. (b) Markers (round black seeds) and two stages of their evolution using the eikonal PDE corresponding to uniform height flooding (contrast criterion). (c) Final segmentation of the flooding in (b). (d) As in (b) but using volume flooding (simultaneous contrast and area criteria). (e) Final segmentation of the flooding in (d).

Acknowledgements

Research support during writing of this chapter was provided in part by the European Network of Excellence 'MUSCLE' and by the Greek research programs PENED-2001 and Pythagoras.

References

[1] L. Alvarez, F. Guichard, P.L. Lions, and J-M. Morel, "Axiomatization et nouveaux operateurs de la morphologie mathematique", *C. R. Acad. Sci. Paris*, pp. 265-268, t.315, Serie I, 1992.

[2] L. Alvarez, F. Guichard, P.L. Lions, and J-M. Morel, "Axioms and Fundamental Equations of Image Processing", *Archiv. Rat. Mech.*, vol. 123 (3), pp. 199–257, 1993.

[3] L. Alvarez and J-M. Morel, "Formalization and computational aspects of image analysis," *Acta Numerica*, pp. 1–59, 1994.

[4] A. Arehart, L. Vincent and B. Kimia, "Mathematical Morphology: The Hamilton-Jacobi Connection", in *Proc. Int'l Conf. Comp. Vision*, pp. 215–219, 1993.

[5] J.A. Bangham, P. Chardaire, C.J. Pye and P.D. Ling, "Multiscale Nonlinear Decomposition: The Sieve Decomposition Theorem", *IEEE Trans. Pattern Anal. Mach. Intellig.*, vol.18, pp.529-539, May 1996.

[6] M. Bardi and M. Falcone, "An Approximation Scheme For The Minimum Time Function", *SIAM J. Control and Optimiz.*, vol.28, pp.950-965, 1990.

[7] G. Barles and C. Georgelin, "A simple proof of convergence for an approximation scheme for computing motions by mean curvature", *SIAM J. Num. Anal.*, vol.32, pp.454-500, 1995.

[8] S. Beucher and F. Meyer, "The Morphological Approach to Segmentation: The Watershed Transformation," in *Mathematical Morphology in Image Processing*, E. R. Dougherty, Ed., Marcel Dekker, New York, 1993, pp.433-481.

[9] H. Blum, "Biological shape and visual science (part I)", *J. Theor. Biol.*, 38, pp.205-287, 1973.

[10] G. Borgefors, "Distance Transformations in Digital Images", *Comp. Vision, Graphics, Image Process.*, 34, pp.344-371, 1986.

[11] R. W. Brockett and P. Maragos, "Evolution Equations for Continuous-Scale Morphology", *Proc. IEEE Int'l Conf. Acoust., Speech, Signal Processing*, San Francisco, CA, March 1992.

[12] R. Brockett and P. Maragos, "Evolution Equations for Continuous-Scale Morphological Filtering", *IEEE Trans. Signal Processing*, vol.42, pp.3377-3386, Dec. 1994.

[13] M. A. Butt and P. Maragos. "Optimal Design of Chamfer Distance Transforms", *IEEE Trans. Image Processing*, vol.7, pp.1477-1484, Oct. 1998.

[14] F. Cao, *Geometric Curve Evolution and Image Processing*, Springer-Verlag, 2003.

[15] V. Caselles, R. Kimmel and G. Sapiro, "Geodesic Active Contours", *Int. J. Comp. Vision*, vol.21, pp.61-79, 1997.

[16] F. Catté, F. Dibos and G. Koepfler, "A Morphological Scheme for Mean Curvature Motion and Applications to Anisotropic Diffusion and Motion of Level Sets," *SIAM J. Num. Analysis*, vol.32, pp.1895-1909, Dec. 1995.

[17] Y.-G. Chen, Y. Giga and S. Goto, "Uniqueness and Existence of Viscocity Solutions of Generalized Mean Curvature Flow Equations," *J. Diff. Geometry*, vol.33, pp.749-786, 1991.

[18] L. D. Cohen, "On Active Contour Models and Balloons", *Comp. Vision, Graphics & Image Processing: Image Understanding*, 53(2): 211-218, Mar. 1991.

[19] M. G. Crandall and P-L. Lions, "Viscosity solutions of Hamilton-Jacobi equations", *Trans. Amer. Math. Soc.*, vo.277, pp.1-42, May 1983.

[20] P-E. Danielsson, "Euclidean Distance Mapping", *Comp. Graphics & Image Process.*, vol.14, pp.227-248, 1980.

[21] L. Dorst and R. van den Boomgaard, "Morphological Signal Processing and the Slope Transform", *Signal Processing*, vol.38, pp.79-98, July 1994.

[22] D. E. Dudgeon and R. M. Mersereau, *Multidimensional Digital Signal Processing*, Prentice Hall, NJ, 1984.

[23] L. C. Evans, "Convergence of an algorithm for mean curvature motion", *Indiana Univ. Math. Journal*, vol.42, pp.553-557, 1993.

[24] L. C. Evans and J. Spruck, "Motion of Level Sets by Mean Curvature. I," *J. Diff. Geom.*, vol.33, pp.635-681, 1991.

[25] M. Falcone, T. Giorgi and P. Loreti, "Level Sets of Viscocity Solutions: Some Applications to Fronts and Rendez-vous Problems", *SIAM J. Appl. Math.*, vol.54, pp.1335-1354, Oct. 1994.

[26] F. Guichard and J-M. Morel, "Geometric Partial Differential Equations and Iterative Filtering," in *Mathematical Morphology and Its Applications to Image and Signal Processing* (H. Heijmans and J. Roerdink, Eds.), Kluwer Acad. Publ., 1998, pp.127-138.

[27] F. Guichard and J.-M. Morel, *Image Analysis and P.D.E.s*, book to be published.

[28] H.J.A.M. Heijmans, *Morphological Image Operators*, Acad. Press, Boston, 1994.

[29] H.J.A.M. Heijmans and P. Maragos, "Lattice Calculus and the Morphological Slope Transform", *Signal Processing*, vol.59, pp.17-42, 1997.

[30] H.J.A.M. Heijmans and R. van den Boomgaard, "Algebraic Framework for Linear and Morphological Scale-Spaces", *J. Visual Commun. and Image Repres.*, vol.13, pp.269-301, 2002.

[31] B.K.P. Horn, *Robot Vision*, MIT Press, Cambridge, MA, 1986.

[32] C. T. Huang and O. R. Mitchell, "A Euclidean Distance Transform Using Grayscale Morphology Decomposition", *IEEE Trans. Pattern Anal. Mach. Intellig.*, vol.16, pp.443-448, Apr. 1994.

[33] P.T. Jackway and M. Deriche, "Scale-Space Properties of the Multiscale Morphological Dilation-Erosion", *IEEE Trans. Pattern Anal. Mach. Intellig.*, vol.18, pp.38-51, Jan. 1996.

[34] B. B. Kimia, A. Tannenbaum, and S. W. Zucker, "'Shapes, Shocks, and Deformations-I: The Components of Two-dimensional Shape and The Reaction-Diffusion Space", *Int. J. Comput. Vision*, 1995.

[35] R. Kimmel and A. M. Bruckstein, "Tracking level sets by level sets: A method for solving the shape from shading problem", *Comp. Vis. Image Understanding*, 62(2):47-58, July 1995.

[36] R. Kimmel, N. Kiryati, and A. M. Bruckstein, "Sub-Pixel Distance Maps and Weighted Distance Transforms", *J. Math. Imaging and Vision*, 6, pp.223-233, 1996.

[37] J. J. Koenderink, "The Structure of Images", *Biol. Cybern.*, 50, pp.363-370, 1984.

[38] P. D. Lax, "Hyperbolic Systems of Conservation Laws and the Mathematical Theory of Schock Waves", SIAM, Philadelphia, 1973.

[39] G. Levi and U. Montanari, "A Grey-Weighted Skeleton", *Information and Control*, 17, pp.62-91, 1970.

[40] P-L. Lions, *Generalized solutions of Hamilton-Jacobi equations*, Pitman Advanced Publ., London, 1982.

[41] R. Malladi, J. A. Sethian, and B. C. Vemuri, "A Fast Level Set Based Algorithm for Topology-Independent Shape Modeling," *J. Math. Imaging and Vision*, vol.6, pp.269-289, 1996.

[42] P. Maragos, "A Representation Theory for Morphological Image and Signal Processing," *IEEE Trans. Pattern Anal. Machine Intellig.*, vol.11, pp.586-599, June 1989.

[43] P. Maragos, "Pattern Spectrum and Multiscale Shape Representation", *IEEE Trans. Pattern Anal. Mach. Intellig.*, vol.11, pp.701-716, July 1989.

[44] P. Maragos, "Morphological Systems: Slope Transforms and Max–Min Difference and Differential Equations", *Signal Processing*, vol.38, pp.57-77, July 1994.

[45] P. Maragos, "Differential Morphology and Image Processing" *IEEE Trans. Image Processing*, vol.78, pp.922-937, June 1996.

[46] P. Maragos, "Algebraic and PDE Approaches for Lattice Scale-Spaces with Global Constraints", *Int'l J. Comp. Vision*, vol.52 (2/3) pp.121-137, May 2003.

[47] P. Maragos and M. A. Butt, "Curve Evolution, Differential Morphology, and Distance Transforms Applied to Multiscale and Eikonal Problems", *Fundamenta Informaticae*, vol.41, pp.91-129, 2000.

[48] P. Maragos and F. Meyer, "Nonlinear PDEs and Numerical Algorithms for Modeling Levelings and Reconstruction Filters", Lec. Notes Comp. Science vol. 1682 (Proc. Scale-Space'99), Springer-Verlag, 1999, pp.363-374.

[49] P. Maragos and R. W. Schafer, "Morphological Systems for Multidimensional Signal Processing", *Proc. IEEE*, vol.78, pp.690-710, Apr. 1990.

[50] D. Marr, *Vision*, Freeman, San Francisco, 1982.

[51] G. Matheron, *Random Sets and Integral Geometry*, Wiley, New York, 1975.

[52] J. Mattioli, "Differential Relations of Morphological Operators", *Proc. Int'l Workshop on Math. Morphology and its Application to Signal Processing*, Barcelona, Spain, May 1993.

[53] B. Merriman, J. Bence, and S. Osher, "Diffusion generated motion by mean curvature", *Computational Crystal Growers Workshop*, J.E. Taylor, editor, (Amer. Math. Soc.), pp.73-83, 1992.

[54] F. Meyer, "Topographic Distance and Watershed Lines", *Signal Processing*, vol.38, pp.113-125, July 1994.

[55] F. Meyer and P. Maragos, "Multiscale Morphological Segmentations Based on Watershed, Flooding, and Eikonal PDE", Lec. Notes Computer Science vol. 1682 (Proc. Scale-Space'99), Springer-Verlag, 1999, pp.351-362.

[56] F. Meyer and P. Maragos, "Nonlinear Scale-Space Representation with Morphological Levelings", *J. Visual Communic. and Image Representation*, vol.11, pp.245-265, 2000.

[57] L. Moisan, "Affine Plane Curve Evolution: A Fully Consistent Scheme", *IEEE Trans. Image Process.*, vol.7, pp.411-420, Mar. 1998.

[58] P. F.M. Nacken, "Chamfer Metrics, the Medial Axis and Mathematical Morphology", *J. Math. Imaging and Vision*, vol.6, pp.235-248, 1996.

[59] L. Najman and M. Schmitt, "Watershed of a Continuous Function", *Signal Processing*, vol.38, pp.99-112, July 1994.

[60] H.T. Nguyen, M. Worring and R. van den Boomgaard, "Watersnakes: Energy-driven Watershed Segmentation", *IEEE Trans. Pattern Anal. Mach. Intellig.*, vol. 25, pp.330-342, Mar. 2003.

[61] S. Osher and J. Sethian, "Fronts Propagating with Curvature-Dependent Speed: Algorithms Based on Hamilton-Jacobi Formulations", *J. Comput. Physics*, 79, pp.12-49, 1988.

[62] S. Osher and R. Fedkiw, *Level Set Methods and Dynamic Implicit Surfaces*, Springer-Verlag, 2003.

[63] K.-R. Park and C.-N. Lee, "Scale-Space Using Mathematical Morphology", *IEEE Trans. Pattern Anal. Mach. Intellig.*, vol.18, pp.1121-1126, Nov. 1996.

[64] Y. Pnueli and A. M. Bruckstein, "DigiDürer - a digital engraving system", *The Visual Computer*, 10, pp.277-292, 1994.

[65] F. Preteux, "On a Distance Function Approach for Gray-Level Mathematical Morphology", in *Mathematical Morphology in Image Processing*, (E.R. Dougherty, Ed.,) Marcel Dekker, NY, 1993.

[66] R. T. Rockafellar, *Convex Analysis*, Princeton Univ. Press, Princeton, 1970.

[67] A. Rosenfeld and J. L. Pfaltz, "Distance Functions on Digital Pictures", *Pattern Recognition*, 1, pp.33-61, 1968.

[68] E. Rouy and A. Tourin, "A Viscocity Solutions Approach to Shape from Shading", *SIAM J. Numer. Anal.*, vol.29 (3), pp.867-884, June 1992.

[69] P. Salembier and J. Serra, "Flat Zones Filtering, Connected Operators, and Filters by Reconstruction", *IEEE Trans. Image Process.*, vol.4, pp.1153-1160, Aug. 1995.

[70] G. Sapiro, R. Kimmel, D. Shaked, B. Kimia, and A. Bruckstein, "Implementing Continuous-scale Morphology via Curve Evolution", *Pattern Recognition*, 26(9), pp.1363-1372, 1993.

[71] G. Sapiro and A. Tannenbaum, "Affine Invariant Scale-Space," *Int'l J. Comp. Vision*, vol.11, pp.25-44, 1993.

[72] M. Schröder, "The Eikonal Equation", *Math. Intelligencer*, 1, pp.36-37, 1983.

[73] J. Serra, *Image Analysis and Mathematical Morphology*, Acad. Press, NY, 1982.

[74] J. A. Sethian, *Level Set Methods and Fast Marching Methods*, Cambridge Univ. Press, 1999.

[75] A. Sofou and P. Maragos, "PDE-based Modeling of Image Segmentation Using Volumic Flooding", in *Proc. ICIP-2003*, Barcelona, Sep. 2003.

[76] H. Tek and B. B. Kimia, "Volumetric Segmentation of Medical Images by Three-Dimensional Bubbles", *Comp. Vision & Image Understanding*, vol.65 (2) PP.246-258, 1997.

[77] H. Tek and B. B. Kimia, "Curve Evolution, Wave Propagation, and Mathematical Morphology", in *Mathematical Morphology and Its Applications to Image and Signal Processing*, (H. Heijmans and J. Roerdink, Eds.,) Kluwer Acad. Publ., 1998, pp.115-126.

[78] J. N. Tsitsiklis, "Efficient Algorithms for Globally Optimal Trajectories", *IEEE Trans. Autom. Control*, 49 (9): 1528-1538, 1995.

[79] R. van den Boomgaard, *Mathematical Morphology: Extensions towards Computer Vision*, Ph.D. Thesis, Univ. of Amsterdam, The Netherlands, 1992.

[80] R. van den Boomgaard and A. Smeulders, "The Morphological Structure of Images: The Differential Equations of Morphological Scale-Space", *IEEE Trans. Pattern Anal. Mach. Intellig.*, vol.16, pp.1101-1113, Nov. 1994.

[81] P. Verbeek and B. Verwer, "Shading from shape, the eikonal equation solved by grey-weighted distance transform", *Pattern Recogn. Lett.*, 11:618–690, 1990.

[82] L. Vincent, "Exact Euclidean Distance Function by Chain Propagations", in *Proc. Conf. on Comp. Vision and Pattern Recognition*, pp.520-525, Hawaii, 1991.

[83] L. Vincent and P. Soille, "Watershed In Digital Spaces: An Efficient Algorithm Based On Immersion Simulations", *IEEE Trans. Pattern Anal. Mach. Intellig.*, vol.13, pp.583-598, June 1991.

[84] A. P. Witkin, "Scale-Space Filtering", *Proc. Int'l Joint Conf. Artif. Intellig.*, Karlsruhe, Germany, 1983.

[85] A. Yezzi, Jr., S. Kichenassamy, A, Kumar, P. Olver and A. Tannenbaum, "A Geometric Snake Model for Segmentation of Medical Imagery", *IEEE Trans. Med. Imag.*, vol.16, p.199-209, Apr. 1997.